12-2012

SPECTROSCOPIC SIGNATURE FOR BUNDLING, EDGE STATES AND IMPURITIES IN 1D AND 0D MATERIALS

Kiran kumar Lingam
Clemson University, klingam@g.clemson.edu

SPECTROSCOPIC SIGNATURE FOR BUNDLING, EDGE STATES AND IMPURITIES IN 1D AND 0D MATERIALS

A Dissertation
Presented to
the Graduate School of
Clemson University

In Partial Fulfillment
of the Requirements for the Degree
Doctor of Philosophy
Physics

---

by
Kiran Kumar Lingam
December 2012

Accepted by:
Dr. Apparao M. Rao, Committee Chair
Dr. Malcolm Skove
Dr. Jian He
Dr. Kathleen Richardson

ABSTRACT

Study of nanomaterials has gained interest of researchers from various fields of science and technology due to their unique electronic and vibrational properties as compared to their bulk counterparts. In particular, carbon nanotechnology has evolved rapidly over the past few decades and nowadays, carbon nanotubes are used in various fields such as energy storage, electronics *etc*. However, the quest for new properties of this material is never ending and the invention of graphene generated enormous interest in the scientific community due to its excellent properties such as strength, high electron mobility, thermal conductivity *etc*. In this thesis, I aim at gaining better understanding of the electronic properties of carbon nanostructures and also discuss the effect of impurities on the vibrational properties of Bismuth nanorods.

In the case of SWNTs, I have studied the effect of surrounding environment on their electronic properties, in particular Sub-nm SWNTs. Due to their unique electronic and vibrational properties, single walled carbon nanotubes (SWNTs) with sub-nanometer diameters $d \sim 0.5–0.9$ nm have recently gained interest in the carbon community. Using UV–Vis–NIR spectroscopy and ultra-centrifugation, we have conducted a detailed study of the π plasmon energy (present at~5–7 eV) in sub-nm SWNTs as a function of the size of the bundle. We find that the energy of the π plasmon peak E varies with the bundle diameter D_h as $E = (0.023 \text{ eV}) * \ln(D_h/d_o) + 5.37 \text{ eV}$, where $d_o = 0.5$ nm and corresponds to the smallest tube diameter. This is compared with the same data for HiPCo and Carbolex SWNTs of larger diameter (1–1.4 nm) confirming a clear dependence of E on

the bundle size, which is present in addition to the previously reported dependence of E on SWNT diameter d.

In case of graphene, the carbon atoms at the edges of graphene sheet contribute to its electronic properties. This effect becomes more prominent in confined structures such as graphene nanoribbons (GNRs) and graphene quantum dots (GQDs). In case of GQDs, previous reports showed that they exhibit a strong photoluminescence (PL) in visible region upon excitation. However, currently no experimental evidence is reported for the origin of PL in these quantum dots. In this work, based on a combination of synthesis, annealing and PL measurements of GQDs, carbon nano-onions (CNOs) and GNRs, we found the PL of GQDs to be independent of its suspension medium and the chirality of its edges. Since GQDs can also be understood as a highly conjugated aromatic molecules, for comparison, this study also discusses the PL spectra of aromatic molecules, which collectively with the PL spectra of GQDs, GNRs and carbon nano-onions serve as a basis for future theoretical and experimental studies of PL in carbon nanostructures.

Lastly, we studied the effect of impurities on the vibrational properties of Bismuth nanorods. Theoretical calculations predict that Bi should undergo a semimetal-to-semiconductor transition as at least one of its dimensions becomes < 50 nm. This prediction was experimentally confirmed by infrared (IR) absorption spectra, which is largely underlain by transitions between the L (electron) and T (hole) pockets of the Fermi surface. In this work, however, we report that in our nanosize samples, the

observed IR peak positions are practically independent of temperature, which is hard to reconcile with the predicted behavior of the *L*–*T* transition. To help elucidate the origin of these IR peaks, we performed a careful analysis of the IR spectra of Bi nanorods, as well as those of bulk Bi, Bi samples prepared under different conditions and $Bi_2(CO_3)O_2$ using Fourier transform infrared and photoacoustic spectroscopy measurements. We propose that the observed IR peaks in Bi nanorods arise from the oxygen–carbon containing secondary phases formed on the surface of Bi rather than from the Bi itself. We believe that secondary phases must be taken into account on a general basis in modeling the IR spectra of Bi and that the scenario that ascribes these IR peaks solely to the *L*–*T* transitions may not be correct. The results reported herein may also impact the research of Bi-based thermoelectric nanostructures and bulk materials.

DEDICATION

To my parents and friends for their constant encouragement, love and affection without whom this work would not be possible.

ACKNOWLEDGMENTS

I gratefully acknowledge Prof. Apparao M. Rao for his support throughout my course of study. Invaluable discussions with him motivated me hugely as a researcher and encouraged me to move forward. I have learnt a lot from him during our interactions. I would also like to thank Dr. Malcolm Skove and Dr. Jian He for their valuable inputs, suggestions and critiques on my work that only lead to improvement. This work would not be possible without your support. Special thanks to Dr. Kathleen Richardson for serving on my committee and providing valuable feedback. I would also like to thank Dr. Steve Serkiz (Savannah Research National Laboratories), Dr. Narayanan Kuthirummal (College of Charleston) Dr. Pu-Chun Ke and Dr. Brain Powell (Clemson University) with whom I had an opportunity to work with and Dr. Lisa Pfefferle (Yale University) for providing Sub-nm SWNT samples for my studies. I also take this opportunity to thank all my group members for their help and support.

TABLE OF CONTENTS

Table of Contents (Continued) Page

LIST OF TABLES

LIST OF FIGURES

List of Figures (Continued)

Figure Page

List of Figures (Continued)

Figure Page

List of Figures (Continued)

Figure Page

List of Figures (Continued)

Figure Page

List of Figures (Continued)

Figure Page

CHAPTER ONE

INTRODUCTION

Carbon nanotubes

Elemental carbon with six electrons arranged in an electronic configuration of $1s^2$, $2s^2$, *and* $2p^2$ forms the building block for a wide variety of molecules with different chemical and physical properties. This forms the basis for modern organic chemistry. Diamond and graphite are two pure carbon crystalline structures studied decades ago. In diamond, carbon atoms are tetrahedrally bonded to their four nearest neighbors to form an sp^3 hybridized configuration, whereas in the case of graphite, each carbon atom is bonded to three nearest neighbors in a plane forming an sp^2 hybridization with p_z orbitals lying perpendicular to the 2D sheet. Study of different allotropes of carbon has created a whole new branch of nanotechnology due to their unique properties and potential for applications in energy storage, field emission, hydrogen storage, electronics *etc* [1]. Several allotropes of carbon based nano materials such as fullerenes and carbon nanotubes have been developed and studied in great detail over the past decades owing to their exceptional electronic, thermal and mechanical properties [2] [3]. Graphene, which is a single layer of continuously bonded sp^2 hybridized carbon atoms and atomically thin can be considered as the building block of almost all carbon nanomaterials, since diamond like sp^3 bonding is difficult to form. As shown in figure 1.1, fullerenes or buckyballs can be imagined as a graphene sheet bent to form a sphere, whereas as single wall carbon nanotubes (SWNTs) are formed by rolling up a graphene sheet into a

cylinder and stacking up such cylinders concentrically form multi wall carbon nanotubes (MWNTs). Layers of graphene stacked on top of each other form the 'bulk form' of graphene - graphite. Since the microscopic structure of SWNTs is closely related to graphene, to gain insight into SWNT properties, it is important to understand the electronic structure of graphene.

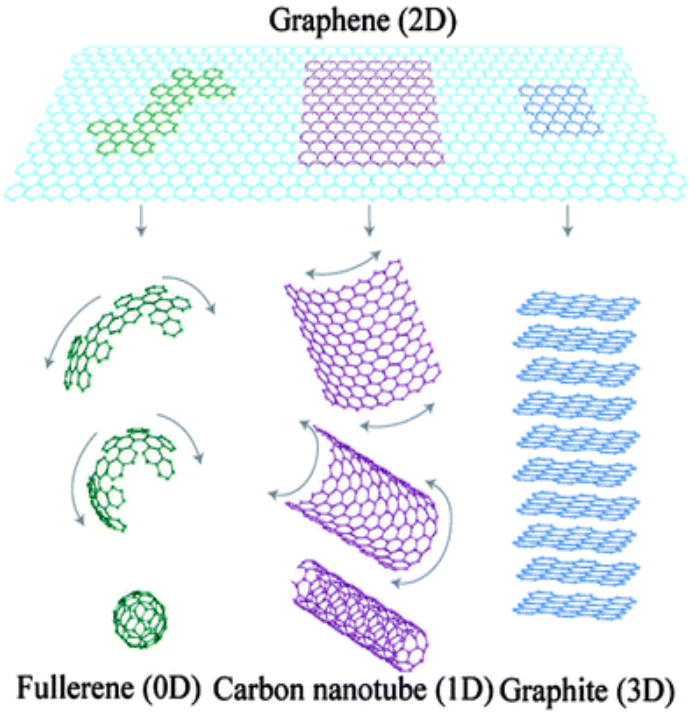

Figure 1.1: Schematic representation of the formation of different carbon allotropes from 2D graphene sheet [4].

As shown in figure 1.2 the dotted lines on the honeycomb lattice of graphene show the section of graphene that can be rolled to form a SWNT, a chiral vector ($\boldsymbol{C}_h$) is used to

specify the dimensions of the nanotube (OA in figure 1.2) and it is defined in terms of the chiral indices *(n,m)*. *n* and *m* denote the relative positions of the a pair of carbon atoms along the unit vectors $\boldsymbol{a_1}$ and $\boldsymbol{a_2}$ axis on a graphene sheet and θ is the chiral angle that corresponds to the angle in which a nanotube is rolled up.

$$\bar{C}_h = n\bar{a}_1 + m\bar{a}_2 \tag{1.1}$$

Where $\boldsymbol{a_1}$ and $\boldsymbol{a_2}$ can be expressed in Cartesian coordinates as

$$\bar{a}_1 = \left(\frac{\sqrt{3}}{2}a, \frac{a}{2}\right); \bar{a}_2 = \left(\frac{\sqrt{3}}{2}a, -\frac{a}{2}\right) \tag{1.2}$$

Where $\left|\bar{a}_1\right| = \left|\bar{a}_2\right| = \left|\bar{a}\right| = \sqrt{3}a_{c-c}$, a is the lattice constant and $a_{c\text{-}c}$ is the carbon-carbon bond length (0.142 nm). The diameter of a SWNT is given by the equation:

$$d = \frac{\bar{C}_h}{\pi} = \frac{\sqrt{3}a_{c-c}\sqrt{m^2 + nm + n^2}}{\pi} \tag{1.3}$$

And the chiral angle θ is given by

$$\theta = \tan^{-1}\left[\frac{\sqrt{3}m}{m+2n}\right] \tag{1.4}$$

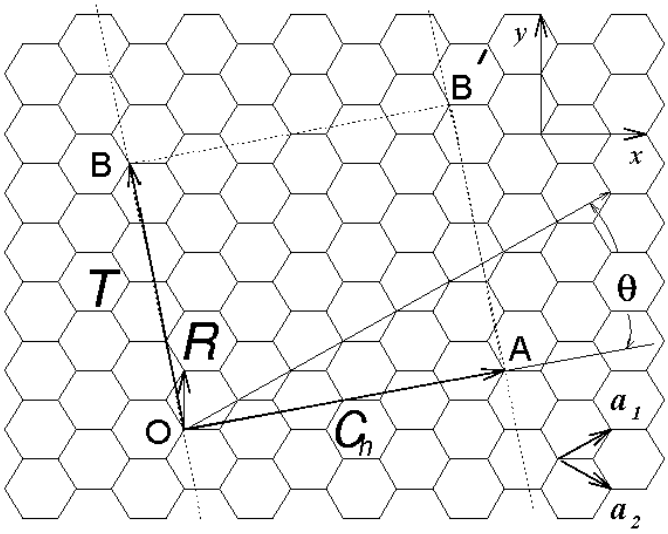

Figure 1.2: An unrolled nanotube projected on a 2D graphene layer, C_h and T represents chiral and the translational vector respectively (along the circumference and along the length of a nanotube) and θ represents the chiral angle [5].

Nanotubes with chiral indices *(n, 0)* and $\theta = 0$ are called "zigzag" tubes whereas $n=m$ in case of "armchair" tubes and all other form of tubes are referred to as chiral tubes. Once we obtain the chiral vector that determines the circumference of the nanotube from *(n, m)* values, the translational vector ***T*** which defines the length of the tube can be drawn perpendicular to the chiral vector; it is given by $T = t_1 \overline{a}_1 + t_2 \overline{a}_2$ where t_1 and t_2 are given by

$$t_1 = \frac{2m+n}{d_R}; t_2 = \frac{2n+m}{d_R} \tag{1.5}$$

Where d_R is the greatest common divisor of $(2n+m)$ and $(2m+n)$ and d_R can be related to the tube diameter d by

$$d_R = \begin{cases} d \text{ if } n\text{-}m \text{ is not a multiple of } 3d \\ 3d \text{ if } n\text{-}m \text{ is a multiple of } 3d \end{cases} \tag{1.6}$$

Due to the difference in geometry, the unit cell of a CNT is not defined by two carbon atoms as in case of graphene, but is given by a rectangle generated by the chiral vector ($\boldsymbol{C}_h$) and translational vector ($\boldsymbol{T}$). The number of hexagons in a unit cell is given by,

$$N = \frac{2(m^2 + nm + n^2)}{d_R} \tag{1.7}$$

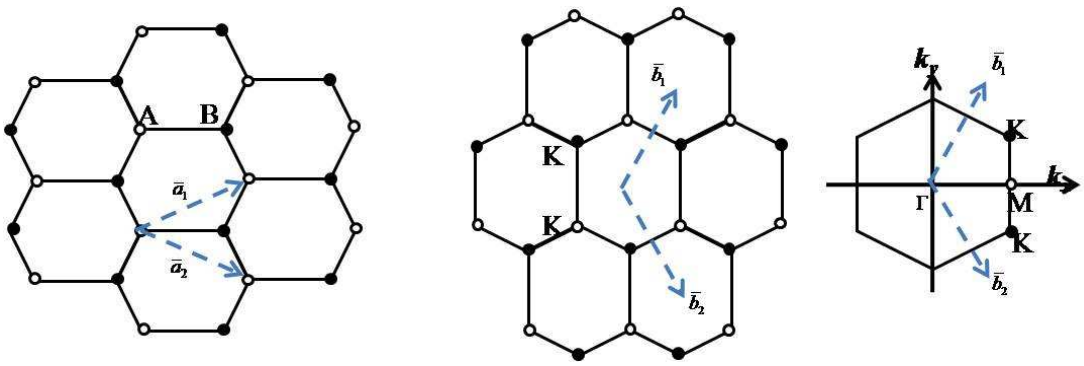

Figure 1.3: The unit cell of graphene in (a) real space and (b) reciprocal space (c) Brillouin zone of graphene with high symmetry points K, M and Γ marked.

In reciprocal space, the unit cell of graphene transforms from *(x,y)* to (k_x, k_y) as shown in figure 1.3. The primitive vectors $\boldsymbol{a_1}$ and $\boldsymbol{a_2}$ in real space are transformed into $\boldsymbol{b_1}$ and $\boldsymbol{b_2}$ in reciprocal space where $\boldsymbol{b_1}$ and $\boldsymbol{b_2}$ are given by

$$b_1 = \left(\frac{2\pi}{\sqrt{3}a}, \frac{2\pi}{a}\right); b_2 = \left(\frac{2\pi}{\sqrt{3}a}, -\frac{2\pi}{a}\right) \tag{1.8}$$

Similarly, a nanotube whose unit cell is given by N can also be reconstructed in reciprocal space. Let $\boldsymbol{k_1}$ and $\boldsymbol{k_2}$ be the reciprocal space vectors orthogonal to $\boldsymbol{T}$ and $\boldsymbol{C_h}$ respectively, such that $\boldsymbol{C_h.k_1=T.\ k_2=2\pi.}$ $\boldsymbol{k_1}$ and $\boldsymbol{k_2}$ can be written in terms of $\boldsymbol{b_1}$ and $\boldsymbol{b_2}$ as $\bar{k}_1 \propto t_2\bar{b}_1 - t_1\bar{b}_2$ and $\bar{k}_2 \propto m\bar{b}_1 - n\bar{b}_2$. The magnitude of $\boldsymbol{k_1}$ and $\boldsymbol{k_2}$ are given by $\left|k_1\right| = \mathbf{2}/d_t$ and $\left|k_2\right| = \mathbf{2}\pi/\left|T\right|$. Combining all the above equations, the expressions for the reciprocal lattice are given by

$$k_1 = \frac{-(t_2\bar{b}_1 - t_1\bar{b}_2)}{N}; k_2 = \frac{(m\bar{b}_1 - n\bar{b}_2)}{N} \tag{1.9}$$

Since $\boldsymbol{k_1}$ and $\boldsymbol{k_2}$ are collinear to $\boldsymbol{T}$ and $\boldsymbol{C_h}$ respectively, the reciprocal lattice of an unrolled nanotube is quantized along $\boldsymbol{k_1}$ and nearly continuous along $\boldsymbol{k_2}$. Based on these values of $\boldsymbol{k_1}$ and $\boldsymbol{k_2}$, "cutting lines" can be drawn aligned along the tube axis. This method of constructing 1D electronic states by cutting the 2D electronic dispersion relations is known as "zone-folding". The number of lines along the tube axis is given by μk_1 and μ is an integer varying from *(1-N/2)* to *N/2*. If these cutting lines pass through the high symmetry *K* point of the Brillouin zone (see Fig 1.3), the nanotubes can be considered metallic, which are otherwise semiconducting [5, 6].

Optical Properties of SWNTs

Widely used spectroscopic techniques such as absorption, emission and Raman spectroscopy have proven to be excellent probes to characterize the electronic and vibrational properties of SWNTs. These experimental tools can provide in depth information about the key parameters such as chirality, diameter and nature of the sample. In this section, we will discuss the absorption mechanism of SWNTs.

It is well known that in graphite *2s, $2p_x$ and $2p_y$* orbitals are strongly bonded by σ bonds while $2p_z$ lies perpendicular to the plane of carbon atoms known as "π" orbital. Generally, σ and π states denote bonding in σ and π orbitals, while σ^* and π^* states corresponds to anti-bonding states. According to Wallace's band model [7], σ, σ^* states are more than 10 eV away from the Fermi energy and only the π and π^* electrons contribute to the electronic conductivity. This energy separation in SWNTs is inversely proportional to the diameter of the tube and the energy values are obtained using tight binding approximation, given by [6]

$$E_{ii} = \frac{2ia_{c-c}\gamma_0}{d} \text{ for semi-conducting tubes and} \qquad (1.10)$$

$$E_{ii} = \frac{6ia_{c-c}\gamma_0}{d} \text{ for metallic tubes} \qquad (1.11)$$

here d is the tube diameter, $a_{c\text{-}c}$ is the carbon-carbon bond length , γ_0 is the overlap integral and i denotes the sub-band number. Figure 1.4 shows the typical energy band

diagrams for metallic and semiconducting nanotubes, where E_{11}^{s} corresponds to an electron excitation from the 1st valance band to the 1st conduction band, E_{22}^{s} refers to the electron excitation from 2nd valance band to 2nd conduction band and so on and E_{11}^{M} corresponds to the first allowed transition in metallic tubes. These values can be derived from the zone-folding scheme using equations (1.10) and (1.11). Since nanotubes are 1D system, their density of states are in form of spikes, called van Hove Singularities (*vHs*) and their band gap is given by $E_{11}^{s} = \frac{2a_{c-c}\gamma_0}{d}$, $E_{22}^{s} = \frac{4a_{c-c}\gamma_0}{d}$ and $E_{11}^{M} = \frac{6a_{c-c}\gamma_0}{d}$.

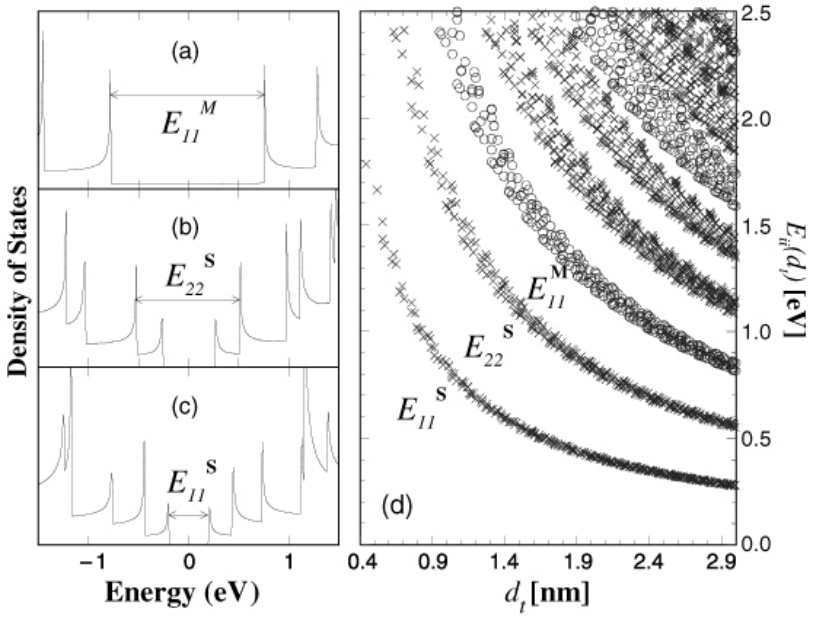

Figure 1.4: (a) shows the 1D density of states for semiconducting and metallic SWNTs and (b) is an empirical kataura plot [8].

In a simplistic picture, for a given diameter of a nanotube, the electronic transition energies can be found using kataura plot (Fig 1.4). Each point in this plot represents one optical transition energy E_{ii} for a tube of particular diameter, d. Although a single nanotube picture is often used to understand the fundamental properties of a nanotube, the system is more complicated in reality. For example, the inter-tube interactions within a nanotube bundle cannot be neglected. Despite the fact that a SWNT has a sharply peaked density of states, the absorption spectrum of SWNTs is generally broad with several peaks buried under a huge envelope. This is due to nanotube bundling. In a nanotube bundle, the tube-tube interactions introduce an electronic dispersion in the direction perpendicular to the plane of nanotube. So, even for a bundle of identical nanotubes, peak broadening is anticipated. During the absorption measurements, an ensemble of nanotubes most often consists of many different species *(n, m)* and different diameters. Due to this bundling effect it is difficult to decouple the signal corresponding to each individual SWNT.

These E_{ii} values are experimentally determined using techniques such as UV-Vis NIR spectroscopy. When the energy of the incident light couples to any of the E_{ii}*'s*, light is absorbed and a peak corresponding to that absorption can be identified in the spectrum. Figure 1.5 shows a typical UV-Vis NIR spectrum of a suspension of SWNTs. In the spectrum, along with the E_{ii}*'s,* another interesting feature can be identified at a higher energy (5.2 eV). This mode is referred to as the π plasmon mode, and arises from

collective excitation of electrons in p_z orbitals. A detailed study of this mode is presented in chapter 3.

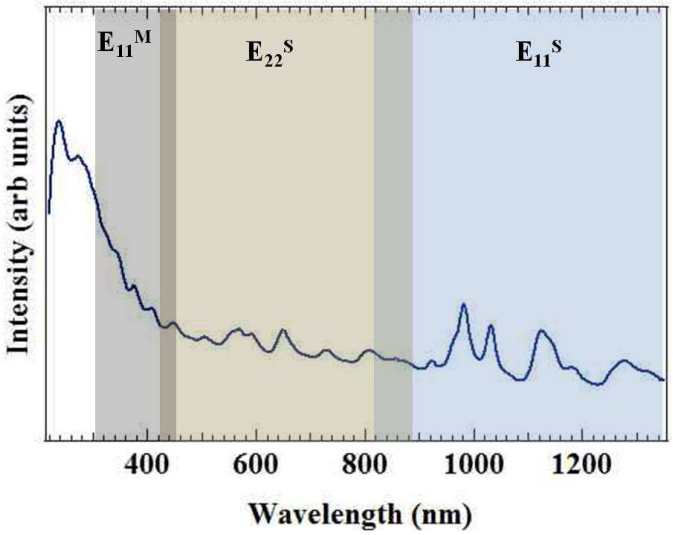

Figure 1.5: Shows the UV-Vis NIR spectrum of SWNTs. The shaded regions correspond to the energies where the electronic transitions corresponding to semiconducting and metallic SWNTs are likely to occur.

Another widely used technique to characterize SWNTs along with the absorption measurements are the photoluminescence (PL) emission studies. In semiconducting SWNTs the electron excited from valance band to conduction band should decay to the ground state. This decay process gives rise to emission of photons with energy lesser than the incident energy. Such emission processes can be observed using PL spectroscopy. In case of SWNTs, these measurements have to be performed when the nanotubes are

isolated in a solution. In a study done by McDonald *et. al.*, they showed that PL intensity is maximum when SWNTs are dispersed and isolated in a surfactant medium and as nanotubes are re-bundled by decreasing the surfactant concentration, PL intensity quenches with a slight upshift in the emission wavelengths due to tube-tube interactions [9].

Graphene

Graphene is a flat land of sp^2 hybridized carbon atoms arranged in the form of hexagons. Each carbon atom is about $a = 1.42\,\text{A}^{\circ}$ from its three neighbors and strongly bonded by σ bonds. The other bond which is oriented in the direction out of the plane is the π bond. These π orbitals can be visualized as a pair of symmetric lobes oriented along the z-axis and centered on the nucleus. Each atom has one of these π-bonds, which are then hybridized together to form what are referred to as the π-band and $\pi*$-bands. These bands are responsible for most of the peculiar electronic properties of graphene [10]. From the band structure of graphene, it can be realized that the valance and conduction bands touch at the K point satisfying a linear E-K relation given by $E(k) = \pm \text{h}\, v_f \sqrt{k_x^2 + k_y^2}$ at the six corners of the Brillouin zone where v_f is the Fermi velocity. Thus the electrons have zero effective mass and the charge carriers obey Dirac equations for spin ½ particles. Hence the linear dispersion at K point is also called the Dirac cone. Despite these fascinating properties, the practical realization of graphene based logic devices has not yet been achieved due to the lack of a band gap in graphene.

For any conventional logic applications, the planar dimensions of graphene must be below 100 nm to open a band gap in its otherwise semi-metallic band structure. To this end, several synthesis techniques including unzipping of carbon nanotubes, chemical vapor deposition and other bottom up fabrication techniques have been reported for the bulk production of graphene nanoribbons (GNRs) and graphene quantum dots (GQDs). These confined systems, such as GNRs have two possible edges, zigzag and armchair. While theoretical models like zone-folding method can be applied to these 1D systems, the presence of the edge states can significantly alter their electronic properties. Recent theoretical and experimental models have shown that GNRs are semiconducting due to edge states and their band gap depends on width of the nanoribbon [11, 12]. Also, the magnetic properties of GNRs can be tuned by edge states [13]. So, a very good understanding of edge physics is crucial to study the properties of these structures.

CHAPTER TWO

SPECTROSOPIC METHODS

Spectroscopy is the most powerful tool to study intrinsic properties of a material such as the energy band structure, defects, excitons, plasmons, phonon modes etc. Modern spectroscopic techniques allow us to scan through the entire electromagnetic spectrum. Even though the basic principle involved for all different spectroscopic methods is very similar in which light is incident on the sample and the output signal is collected using detectors. The choice of incident light energy, instrumentation and optical setup largely depends on the material and the properties that are of interest.

The wide range of optical processes that occur can be broadly classified into three types, reflection, transmission and absorption. When light passes through matter, some part of light is reflected from the front surface while rest of the light is transmitted through the sample, R and T denote these two processes respectively. In an ideal case, R+T would be unity, and the absorption would be zero. However, during the interaction of light with the sample, several other processes take place, yielding information about the sample.

1) When light enters a medium, the light waves are slightly bent at the interface due to change in the refractive index of the medium. Such a phenomenon is called “Refraction”.
2) During the passage of light through the sample, if the energy of the light couples with an electronic transition in the system, some of that particular light energy is absorbed; such a process is called Absorption.

3) It is well known that electrons always tend to exist in the lowest energy level possible. So, an electron that is excited during the absorption process often decays to the ground state. During this relaxation process, energy is emitted, often in the form of a photon. Such a process is known as luminescence.

4) Scattering is another important process, here the incident light is re-directed to other directions after interaction with the sample; some part of light continues forward and some is scattered. Such a scattering process is said to be elastic if there is no frequency change after the interaction and it is non-elastic if the frequency changes. Such non-elastic scattering process provides valuable information about the material. This forms the basis for Raman Spectroscopy [14].

Absorption Spectroscopy

Linear response model and linear response functions provide very good approximations to understand the fundamental properties of solid-state spectroscopy. This model is based on the interaction of a system with an external force and is applicable when the response is linear. For example, the polarization (P) of the system under an incident electric field is given by a response function called electrical susceptibility. Similarly, dielectric function (ε) relates the displacement (D) and the electric field (E). Based on these linear response functions and using standard Maxwell's equations, one can formulate equations for optical constants such as absorption coefficient. Generally, complex refractive index is

the term used to define both absorption and refractive indices of a medium [14] and it is given by

$$\tilde{n} = n + i\kappa \tag{2.1}$$

Where n is the normal refractive index and κ is the extinction coefficient. As shown below, the extinction coefficient is directly related to the absorption coefficient. If the light wave is propagating along the Z direction, the time varying waveform is given by

$$E = E_0 e^{i(kz-\omega t)} \tag{2.2}$$

Where ω corresponds to the frequency and in case of a non-absorbing medium

$$k = \frac{n\omega}{c} \tag{2.3}$$

Here, n is refractive index of the medium. For an absorbing medium, the complex refractive index has to be taken into account

$$k = \frac{\tilde{n}\omega}{c} = \frac{(n+i\kappa)\omega}{c} \tag{2.4}$$

Now, substituting equation (2.4) in (2.2) the electric field can be given by

$$E = E_0 e^{i((n+i\kappa)\frac{\omega}{c}z-\omega t)}$$

$$E = E_0 e^{-\kappa\omega z/c} e^{i(\omega nz/c-\omega t)} \tag{2.5}$$

The non-zero term for excitation coefficient leads to an exponential decay of the wave in the medium. The intensity of light wave passing through the medium is given by

$I \propto EE^*$. So, from equation (2.5)

$$I = e^{\frac{-2\omega\kappa z}{c}} \tag{2.6}$$

This equation describes that the light intensity decays exponentially with a decay constant of $2k\omega/c$. Now, comparing equation (2.6) with Beer Lambert's law $I = I_0 e^{-\alpha z}$, the value for absorption coefficient is given by $\alpha = \frac{4\pi\kappa}{\lambda}$. This relation suggests that the value of absorption coefficient is directly related to the extinction coefficient. Also, from the standard Maxwell's equations, the refractive index of a medium is related to its dielectric function by

$$\tilde{n} = \sqrt{\varepsilon}_r \tag{2.7}$$

Since, $\tilde{n}$ is a complex variable, ε_r is also a complex function of dielectric constant and is also called relative permittivity.

$$\tilde{n} = \sqrt{\varepsilon_1 + i\varepsilon_2} \tag{2.8}$$

$$n + i\kappa = \sqrt{\varepsilon_1 + i\varepsilon_2} \tag{2.9}$$

So, by comparing real and imaginary parts

$$\varepsilon_1 = n^2 - k^2 \quad \text{and} \quad \varepsilon_2 = 2nk \tag{2.10}$$

Writing n and k in terms of ε_1 and ε_2

$$n = \frac{(\varepsilon_1 + (\varepsilon_1^2 + \varepsilon_2^2)^{1/2})^{1/2}}{\sqrt{2}} \text{ and } k = \frac{(-\varepsilon_1 + (\varepsilon_1^2 + \varepsilon_2^2)^{1/2})^{1/2}}{\sqrt{2}} \tag{2.11}$$

Combining all the above equations, the absorption coefficient can be written in terms of imaginary part of dielectric functions as

$$\alpha(\omega) = \frac{\omega.\varepsilon_1(\omega)}{c_0.n(\omega)} \tag{2.12}$$

Quantum Mechanical description of absorption coefficient

From the classical description, it is clear that the absorption coefficient depends on the imaginary part of the dielectric function, however, to understand the mechanism at an atomic scale, we must use a quantum mechanical approach. The probability of transition from the initial state to the final state gives information about the strength of absorption. For this transition to occur, the system has to be perturbed by an external energy, let this be *H'*. Suppose the transition probability from initial state *i* to the final state *f* is given by

$$\left|H'_{fi}(0)\right|^2 \tag{2.13}$$

If the perturbation is in the form of an electromagnetic wave, the time dependent vector potential is given by *A(x,t)* and the perturbation is given by

$$H' = -\frac{e}{m} p\bar{A} \tag{2.14}$$

Where *e* and *m* are the charge and mass of the electron undergoing transition and *p* the momentum operator. It should be remembered that H'_{fi} is an element of the matrix *H'*. Now, for simplicity, let us neglect the higher order perturbations caused by the EM field

and consider only the first order perturbation. Using the *golden rule* of quantum mechanics, we can obtain the probability of transition per unit time, given by,

$$p_{fi} = \frac{2\pi \left| H'_{fi}(0) \right|^2}{\hbar^2} \delta(\omega_{fi} - \omega) \tag{2.15}$$

Now, representing the matrix element (H'_{fi}) in bra-ket notation and including equation (2.15)

$$H'_{fi} = < f \left| H' \right| i > = -\frac{e}{m} < f \left| p\overline{A} \right| i > \tag{2.16}$$

The matrix element above has both time dependent and independent parts. The time dependent part of the matrix element gives delta function in equation (2.16), it is evident that the electronic transition requires energy conservation. For the time independent part, let us consider a dipole approximation so that the vector potential is given by $\overline{A} = A_0 e^{ikx}$ with the amplitude A_0, from equation (2.16)

$$H'_{fi}(0) = -\frac{eA_0}{m} < f \left| p \right| i > = -\frac{eA_0}{m} p_{fi} \tag{2.17}$$

The momentum matrix element in the above equation can be expressed in the momentum representation as

$$(p_j)_{fi} = -i\hbar \int \psi_f^* \frac{\partial \psi_i}{\partial x_j} d^3x \tag{2.18}$$

The perturbation matrix element in equation (2.18) is given by

$$(H_j)'_{fi} = \frac{i\hbar e A_0}{m} \int \psi_f^* \frac{\partial \psi_i}{\partial x_j} d^3x \tag{2.19}$$

From the Heisenberg equation of motion, the momentum matrix element and the dipole matrix can be related by the equation,

$$p_{fi} = \frac{im\omega_{fi}}{e}(M_j)_{fi} = i\omega_{fi}\frac{m}{e}\int \psi^*_f ex_j \psi_i \, d^3x \tag{2.20}$$

M_{fi} is the matrix element for the dipole moment ex_{fi} dipole; the transition matrix element can be expressed in dipole representation by replacing the momentum matrix element with dipole matrix element. Using equation (2.17), the transition probability from the initial state to final state is given by

$$\left|H'_{fi}\right|^2 = \left|< f\left|H\right|i >\right|^2 = \frac{e^2 A_0}{m^2}\left|< f\left|p\right|i >\right|^2 \tag{2.21}$$

Applying fundamental principles of electrodynamics, the square of the vector potential can be written in terms of intensity as

$$I(\omega) = nA_0^2 \varepsilon_0 c_0 \omega^2 \tag{2.22}$$

So, from equation (2.21) and (2.22) the perturbation element is

$$\left|H'_{fi}\right| = \frac{e^2 I(\omega)\left|p_{fi}\right|^2}{m^2 \varepsilon_0 c_0 \omega^2 n} \tag{2.23}$$

Now, these values are derived for one electronic transition from initial to final states and validating energy conservation laws. For a transition between levels in a semiconductor, a summation of such transitions is required and the energy and momentum should be conserved.

Absorption can be given as the ratio of energy absorbed per unit volume (v) to the energy incident per unit area and is given by [15]

$$\alpha(\omega) = \frac{\hbar\omega P_{fi}}{I(\omega)v} \tag{2.24}$$

Combining the above equations (2.16), (2.23) and (2.24)

$$\alpha(\omega) = \frac{2\pi}{v} \frac{e^2 \left| P_{fi} \right|^2}{m_0^2 \varepsilon_0 c_0 n\omega} \delta(\hbar\omega_{fi} - \hbar\omega) \tag{2.25}$$

Combining equation (2.12) and (2.25), the imaginary part of dielectric function can be expressed as

$$\varepsilon_1(\omega) = \frac{2\pi}{v} \frac{e^2 \left| p_{fi} \right|^2}{m_0^2 \varepsilon_0 \omega^2} \delta(\hbar\omega_{fi} - \hbar\omega) \tag{2.26}$$

Instrumentation

UV-Vis NIR (ultraviolet-visible-near infrared) spectroscopy is one of the most commonly used spectroscopic techniques to study the absorption properties of a sample. The basic parts of a spectrophotometer are a light source, a holder for the sample, monochromators, and a detector. Tungsten or Xenon lamps are often used as source and a photo multiplier tube (PMT) or a charge-coupled device (CCD) used to detect the signal. A diffraction grating is used to scan through all the excitation wavelengths. Each wavelength passes through the sample in the sample holder. Depending on the sample, absorption intensity

fluctuates and finally the intensity of the spectrum is recorded as a function of wavelengths.

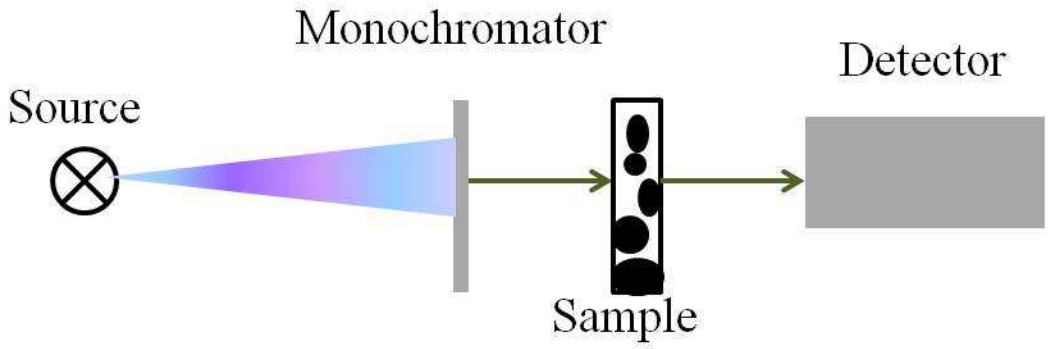

Figure 2.1: A schematic diagram showing UV-Vis- NIR spectrometer setup.

These UV-Vis NIR spectroscopic measurements are mostly done on liquid samples and intensity of light absorbed also depends on the concentration of the sample in the solvent. A correlation between the solution concentration and absorbance can be obtained using Beer-Lambert's law

$$A = \kappa lc$$

Where κ is the molar absorptivity (extinction coefficient), c is the concentration of the solution and l is the cell path length.

Photoluminescence Spectroscopy

In this section, we look into the luminescence of materials which is the counterpart of absorption. Any electron excited to higher levels tends to come back to its lowest energy,

ground state. Such a relaxation process is termed as luminescence. However, the luminescence process is not as straight forward as absorption, because an electron can decay to its ground state in several possible ways, some radiative and some non-radiative. The probability that the excitation has multiple steps is small. To understand this phenomenon, information about the energy band diagrams of the sample is important. In a bulk semiconducting material, the conduction band and valance band are separated by an energy gap also known as band gap. These energy levels are nearly continuous. If the electrons are excited to higher levels in a conduction band, the electrons will not stay there for long and tend to attain the lowest energy possible in the conduction band by emitting phonons. Such a phonon emission process continues till the excited electron reaches the bottom of the conduction band, after which the electron emits photons and relaxes to the top of the valence band, its ground state. Thus the lowest level in the conduction band and highest level of valance band (as well as the occupation) are very important to understand photoluminescence. For 1D materials like SWNTs, nanoparticles, nanowires or for 0D materials such as quantum dots, the energy levels are discrete and the tip of valance band and conduction band are referred to as Highest Occupied Molecular Orbitals (HOMO) and Lowest Unoccupied Molecular Orbitals (LUMO) levels respectively.

The electrons in the ground state of a molecule often have anti parallel spins and are hence paired up with total spins $S=0$ (singlet state). After excitation, an unpaired electron in an excited state and an unpaired electron in the ground state may have their spins either

parallel (*S=1*) or anti parallel (*S=0*) to each other and hence can either form a singlet or a triplet state. These singlet and triplet states are very important to determine the optical properties of a material. As mentioned, relaxation processes are complicated and a Perrin-Jablonski diagram is widely used to explain the different processes involved such as absorption, internal conversion, intersystem crossing, fluorescence, or phosphorescence. In the diagram S_x ($x=0, 1, 2$) corresponds to the singlet electronic state while T_x ($x=1, 2$) corresponds to the triplet electronic states and the possible relaxation processes are

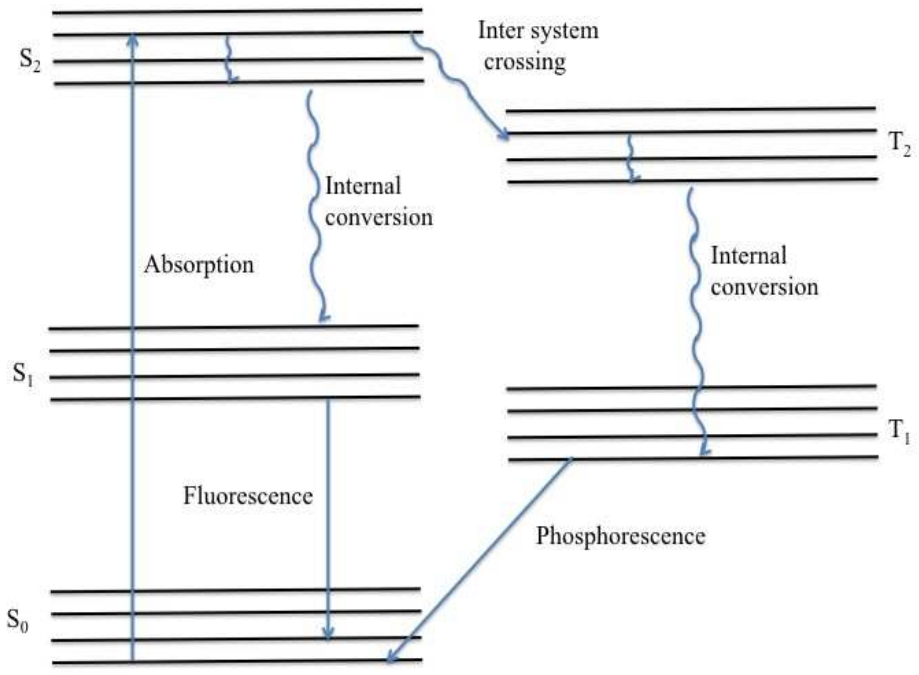

Figure 2.2: Jablonski diagram showing the singlet and triplet electronic states and the corresponding electron relaxation processes.

1) *Internal Conversion*: This is a non-radiative decay process in which the excited electron jumps from a higher vibrational level to a lower vibrational level by emitting phonons. This process occurs within the electronic states with same spin multiplicity.
2) *Fluorescence*: This is most common form of electron decaying process; photons are emitted during this process. An excited electron always decays to its lowest first excited state by non-radiative processes before relaxing to the ground state by emitting photons. So, in most cases the fluorescence occurs at a lower energy than the corresponding absorption.
3) *Inter system crossing*: This process occurs between iso-energetic vibrational states with different spin multiplicity. Generally, electronic transitions between same spin multiplicities are allowed whereas transitions between different spin multiplicities are forbidden. But, such a forbidden process is bound to happen during inter system crossing due to spin orbit coupling. So, an electron in a singlet state can move to a triplet state of the same energy before decaying to the ground state.
4) *Phosphorescence:* An electron which jumped into a triplet state will reside there for a long time before it decays to the ground state. Such an emission process is called Phosphorescence. Usually this is a delayed process compared to Fluorescence.

In most experimental results, the absorption and emission spectra of a sample are broad. This peak broadening can be classified into homogeneous and non-homogeneous broadening. The former is due to the presence of closely packed vibrational sub-levels in each electronic state and the latter is due to the changes in the local electric fields due to interaction within solvent-solute configurations. Along with the processes described above, several external factors, such as the pH and temperature of the medium, affect the fluorescence of the sample. On the other hand, several other dynamic processes such as static quenching, dynamic quenching, formation of excimers and several other charge transfer mechanisms can lead to changes in the fluorescence efficiency of the sample [16].

A typical setup for photoluminescence measurements is similar to that for absorption measurements. A Xenon or Tungsten lamp is used as a light source, light is dispersed and the desired wavelength light is sent to the sample using monochromators. The emitted light from the sample is collected using PMT or CCD detectors. The intensity of emitted light is plotted as a function of emission wavelength.

Fourier Transform Infrared Spectroscopy

Infrared spectroscopy is one of the most powerful spectroscopic tools for material characterization. This technique allows us to probe into the far IR, mid IR and near IR regions of the electromagnetic spectrum. Using this technique along with UV-Vis-NIR

spectroscopy could provide nearly complete fundamental information regarding the electronic structure of a material. Along with the absorption processes such as electronic transitions between energy levels, defects or excitons, FTIR spectroscopy also provides insight into other absorption and reflection processes such as IR active phonon modes and vibrational modes. These results combined with other techniques like Raman spectroscopy could yield nearly complete information about the vibrational properties of a material. Using FTIR spectrum, the composition of the molecules in a hetero-atomic compound can also be identified from the vibrational frequencies and phonon modes. However, not all phonon modes are active in FTIR spectroscopy, knowledge of group theory and symmetry vibrations is necessary to assign infrared bands to a particular vibrational mode.

Any two atoms are bonded together with a specific bond length. Depending on their arrangement within the molecule, they can have several degrees of freedom. A polyatomic molecule with N atoms will have 3N degrees of freedom, for a molecule with symmetric structure some modes are indistinguishable from each other and such modes are said to be degenerate. Linear molecules are the best examples for such systems. On the other hand, in some molecules all the modes are distinguishable, CO_2 and H_2O are simple examples of such cases. H_2O being a non-linear molecule, will have 3 degrees of freedom for translational motion and 3 for rotational motion. On the other hand, in case of CO_2, it has 3 degrees of freedom in translational motion and 2 degrees of freedom in rotational motion , because the rotation around O=C=O is degenerate.

Depending on the structure of a molecule, some vibrations involve changes in the bond length and bond angle, and can be symmetric or asymmetric. Complete information about these vibrations can be obtained from the character table generated using group theory. During some vibrations, the dipole moment of the molecule changes and such vibrations cause an IR active mode. The more the strength of vibrations, the more intense the corresponding band in the spectrum. Generally, asymmetric molecules have higher IR active modes compared to a symmetric molecule due to higher probability of changes in the dipole moment in the former.

Instrumentation

The principle of operation of an FTIR spectrometer is based on the interference of two light waves based on Michelson interferometry. The schematic diagram shows a simple setup. The light beam coming from the source is bisected by the beam splitter. 50% of the light is deflected and falls on M1; this is reflected again from M1 and passes through the beam splitter. While the rest of light is transmitted through the beam splitter and falls on a moving mirror M2, light reflected from M2 returns to the beam splitter, an interference pattern is created due to the difference in the path lengths created by two mirrors. Depending on the displacement of M2, it can form a constructive or destructive interference. This recombined beam passes through the sample; light is absorbed by the sample depending on the properties of the material.

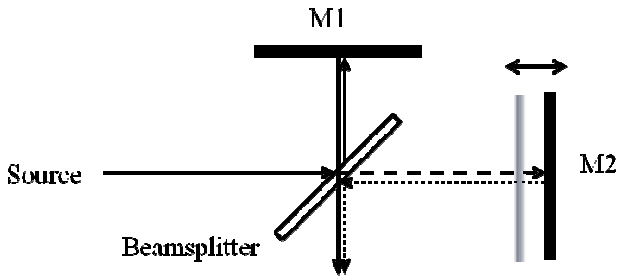

Figure 2.3: Schematic representation of a Michelson interferometer.

CHAPTER THREE

EFFECT OF BUNDLING ON THE π PLASMON ENERGY IN SUB-NANOMETER SINGLE WALL CARBON NANOTUBES

As explained in Chapter 1, a single wall carbon nanotube (SWNT) is a well known quasi one-dimensional system whose physical properties depend on the tube diameter and chirality. These SWNTs tend to form ropes or bundles due to strong intertube Van der Waals interactions. Spectroscopic studies on such bundles failed to show a well resolved spectrum due to overlapping peaks resulting from the interactions between bundled tubes in side-by-side Van der Waals (Vdw) contact. Thus, researchers have focused on isolating or de-bundling these SWNTs by preparing stable dispersions of SWNTs in different solvents such as polymers, DNA and using ionic and nonionic surfactants. Observation of vibrational and electronic properties of an isolated nanotube provides a greater insight into the physics of these materials than a nanotube bundle does, due to the fact that a nanotube bundle usually consists of mixed chiralities and diameters, as well as the forementioned VdW interactions. So, the tube-tube interactions are crucial in determining properties of SWNTs.

Effect of Bundling on the vibrational properties of 1D and 2D carbon systems

Study of phonon modes in carbon systems like C_{60}, SWNTs and graphene lead to a deep understanding of the vibrational properties of these materials. Among the spectroscopic techniques for investigating vibrational properties, Raman spectroscopy is by far the most

commonly used tool to characterize SWNTs, due to a unique phenomenon called "Resonant Raman scattering". When the incident laser energy matches the band gap of a nanotube, phonon modes are activated giving rise to an enhanced Raman signal even for an isolated SWNT level. A typical Raman spectrum of SWNT samples consists of a Radial Breathing Mode (RBM) at low frequencies resulting from an in phase vibrations of carbon atoms in radial directions, a G band at high frequency arising from the tangential vibrations, a D band associated with the defects in the SWNT samples and overtone modes of these frequencies. The dependence of these vibrational frequencies (**ω)** on the diameter of the nanotube is given by the equation

$$\omega = \omega_0 + \frac{\beta}{d_t^n} \tag{3.1}$$

Where ω_o is the frequency of 2D graphite, and β and n are the coefficient and exponent of the diameter dependence. For the case of graphite or graphene d_t tends to infinity. The RBM frequency determines the nanotube diameter distribution in the sample using the relation $\omega_{RBM} = 224 / d_t + B$ where d_t is the tube diameter and B is the shift in the frequency due to tube-tube interactions. The effect of intertube interactions on the vibrational modes of SWNTs was first reported by Venkateswaran *et al.* where a shift in the frequencies was reported under variable external pressure [17]. Later, Rao *et. al.* determined that a shift of approximately 14 cm^{-1} is possible due to nanotube bundling [18].

Along with ID carbon nanomaterials such as SWNTs, bundling also influences the vibrational properties of 2D materials. In case of graphene, the coupling between adjacent graphene planes is similar to the tube-tube interactions within SWNT bundles. Again, Raman spectroscopy provides valuable information regarding graphene samples. The G band that corresponds to tangential vibrations of carbon atoms and the 2D band, which is the overtone of the defect induced D band are the most prominent peaks in the Raman spectrum of graphene. This 2D band is the most commonly used Raman signature to determine layer thickness and the presence of dopants. For a single layer graphene film, the 2D band is intense and sharp with a FWHM of ~ 25 cm^{-1}, but as the number of layers increase, this 2D band becomes broader with a lower intensity. As the number of layers increase to more than 3 the 2D band splits and forms a two peak structure. These results from 1D and 2D carbon systems provide clear evidence that the VdW interactions are crucial in determining the vibrational properties of these materials.

Effect of Bundling on the electronic properties of SWNTs

As discussed earlier, the electronic properties of SWNTs are mainly governed by E_{ii}*'s* where the energy gap for the first (E^S_{11}) and second (E^S_{22}) pairs of Van Hove singularities in the electron density of states for semiconducting SWNTs range between 0.79 - 1.48 eV and 1.39 - 2.5 eV [19]. In metallic SWNTs, E^M_{11} transitions are present in the range 2.0 - 3.1 eV [20]. All these spectral features greatly depend on the diameter and chirality of the nanotube. In addition to these inter-band transitions E_{ii}, UV-Vis-NIR and electron energy

loss spectroscopy (EELS) have reported high energy features around 5.2 eV which correspond to collective excitations of π electrons (π plasmon) [21, 22]. In graphite, the carbon atoms exhibit sp^2 hybridization in which each carbon atom is connected evenly to three carbons in the *xy* plane and a weak π bond is present in the *z* direction. This sp^2 set forms the honeycomb lattice of a graphene sheet and the p_z orbitals are responsible for the Van der Waals bonding between graphene sheets. The free electrons in the p_z orbitals are delocalized and behave like an electron cloud [23]. In a SWNT, which is a rolled-up graphene sheet, the carbon-carbon bond becomes more sp^3 like and the p_z orbitals overlap due to the quasi 1D nature of nanotubes. This overlap becomes more significant as the diameter decreases below 1 nm [24]. The energy corresponding to the π plasmon energy depends on the nanotube diameter [25, 26] and the overlap integral [27]. This feature occurs as a result of electronic transition at the M point in the Brillouin zone, whereas the E_{ii}*'s* result from the electronic excitations at the K point (ref. figure 1.3).

Recently, Rance *et al*. [25] reported the dependence of the π plasmon energy on the tube diameter in small SWNT bundles derived from CoMoCAT, HiPCo, electric arc and chemical vapor deposition synthesis methods. An empirical relation given by $E_\pi = 4.80 + 0.70/(d_{\mathrm{NT}})^2$ was also reported where d_{NT} corresponds to the tube mean diameter and E_π is the π plasmon energy. However, their study did not address the effect of de-bundling on the π plasmon energy. Que [28] has proposed that different plasmon modes in a SWNT bundle can couple due to inter tube interaction and result in a shift in the π plasmon energy. In this report we present UV-Vis-NIR data for sub-nm SWNTs (*d*

< 1 nm) with a view towards quantifying the effect of bundling on the π plasmon energy and providing an empirical relation between the π plasmon energy and the SWNT bundle size.

Experimental Section

SWNT bundles used in this work were synthesized using a thermal CVD process with a bimetallic catalyst. Prior to the SWNTs synthesis, CoMn-MCM-41 catalyst with 3% metal loading and a Co:Mn ratio of 1:1 was synthesized by isomorphous substitution of metal in the MCM-41silica template. These MCM-41 templates have an average pore diameter of about 3 nm. The SWNT synthesis was performed in a quartz tube reactor by thermal disproportionation of CO gas at 600 – 800^{o}C under hydrogen at desired synthesis temperatures of 600, 700 and 800^{o}C. In our studies, we refer to these samples as S1, S2 and S3. Characterization techniques such as Transmission Electron Microscopy and Raman Spectroscopy were used to determine the diameter distribution of the sample. The average tube diameters ranged from 0.5 to 0.9 nm. These samples are called sub-nm SWNTs due to their diameters, less than 1 nm. Figure 3.1 shows transmission electron microscope images and the diameter distribution of as-synthesized sub-nm SWNTs [29].

In order to determine the dependence of π plasmon energy on bundle size, we de-bundled the SWNT bundle down to isolated tubes by dispersingthe nanotubes with surfactant. Briefly, we adopted the method described by Arnold *et al.* [30] wherein sub-nm SWNT

bundles were dispersed at a concentration of 1 mg/ml in an aqueous solution containing 2% (w/v) sodium cholate (SC). About 3 ml of this solution was bath sonicated (Aquasonic Inc., model P250HT) for 1 h and followed with centrifugation (Beckman coulter ultracentrifuge, TLA 100.3 rotor, 158,000 *g* max) for different centrifuge times (5, 15, 30, 45 and 60 min). During the sonication process, the surfactant molecules bind to the nanotube surface. When the SWNT bundle is broken by the energy supplied during ultrasonication, small bundles/isolated SWNTs are collected at the top of the solution during centrifugation. After centrifugation, the top 70% of the supernatant was de-canted for our studies.

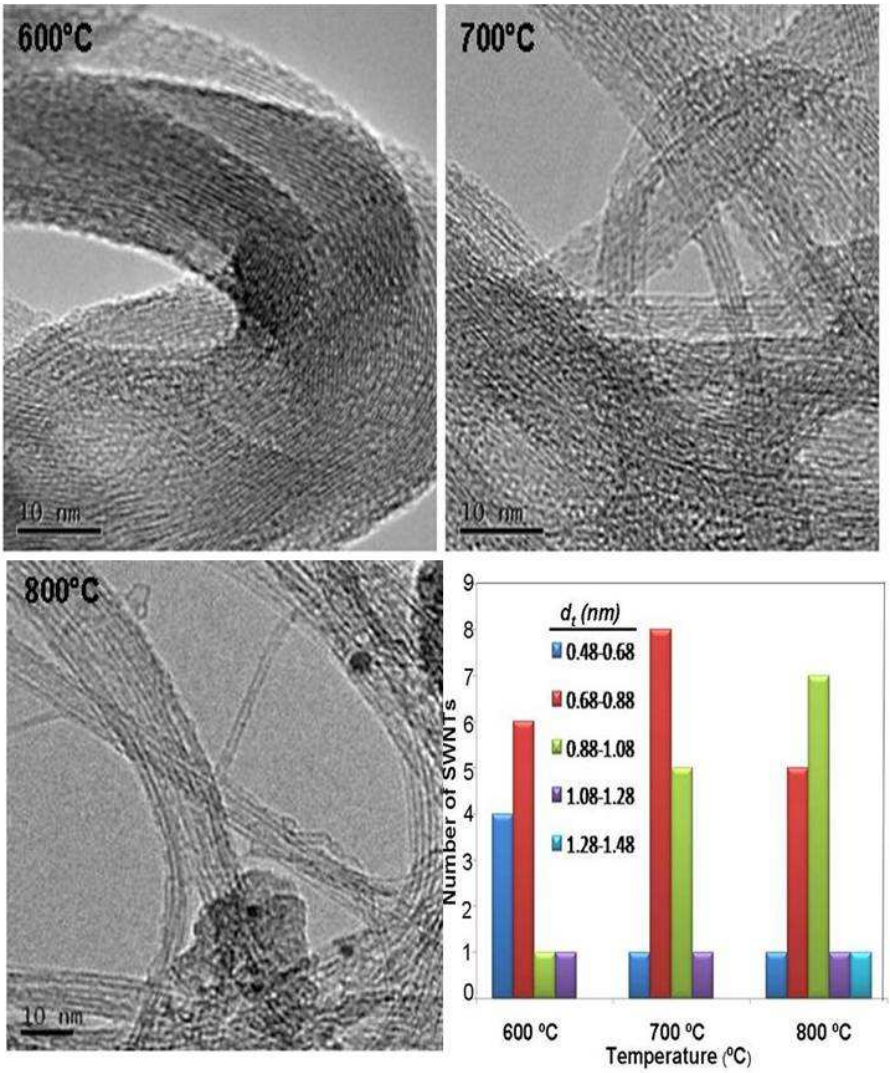

Figure 3.1: (a), (b) and (c) show the Transmission Electron Microscopy images of sub-nm SWNTs synthesized at 600, 700 and 800^{0}C. (d) The diameter distribution of these samples obtained from TEM and Raman spectroscopy.

Results and Discussion

Figure 3.2 shows the UV-Vis-NIR spectra of as-prepared samples of S1, S2 and S3 before and after centrifugation for 15 and 60 min. Each of the absorption peaks corresponds to an electronic transition energy in semiconducting or metallic sub-nm SWNTs, The peak positions are governed by the equations $E_{11}^{s} = \frac{2a_{c-c}\gamma_0}{d}$, $E_{22}^{s} = \frac{4a_{c-c}\gamma_0}{d}$ and $E_{11}^{M} = \frac{6a_{c-c}\gamma_0}{d}$, where $a_{c\text{-}c}$ is the carbon-carbon bond length, γ_0 the overlap integral and d the tube diameter. After centrifugation for 15 min to 60 min, the peaks corresponding to E_{ii} from individual sub-nm SWNTs within the bundle become pronounced and discernable inside the broad absorption spectrum for the bundled samples. This observation is attributed to a decrease in the bundle size with increasing centrifugation time.

The shaded region in Figure 3.2 highlights the region where electronic transitions due to metallic nanotubes are expected. It is evident that more peaks are present in the metallic region for S3 than in S1. This is consistent with the previous observations on the same samples which showed that low temperature (600^{o}C) favors minimal growth of metallic nanotubes [29]. Furthermore, combined photoluminescence and Raman studies on these sub-nm SWNTs showed that the dominant tube present in S1, S2 and S3 is the (6, 5) semiconducting nanotube. The intense peaks present in Fig. 3.2 at 985 nm correspond to (6, 5) nanotubes, consistent with previous report.

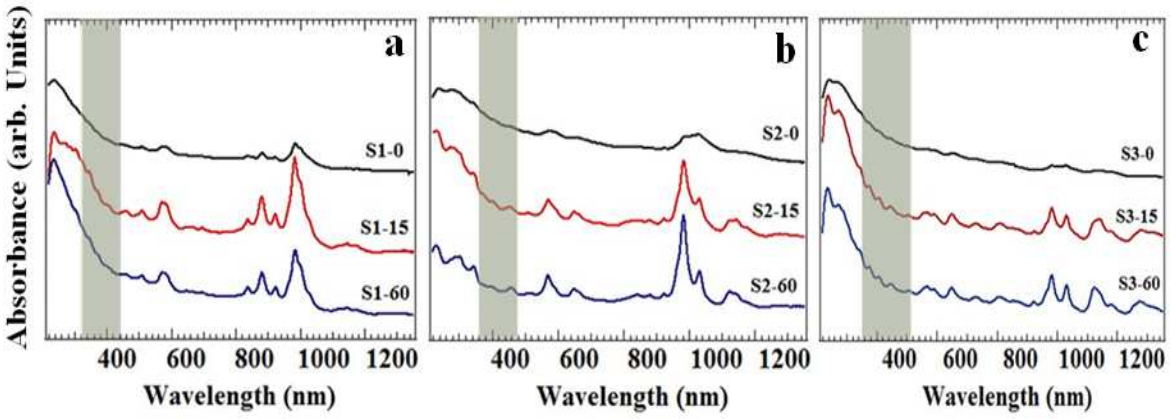

Figure 3.2: Comparison of UV–Vis–NIR spectra of bundled samples: (a), S1 was grown at 600 ^{o}C (b) S2 at 700 ^{o}C and (c) S3 at 800 ^{o}C. Here black curve shows spectra of uncentrifuged SWNTS, red and blue traces show the spectra after centrifugation for 15 min, 60 min respectively. The shaded area is where electronic transitions due to metallic nanotubes are expected.

In SWNTs, the π band is formed by the overlapping $2p_z$ orbitals resulting in the π plasmon peak which appears at ~ 5-7 eV in the UV-Vis-NIR spectrum [31]. Figure 3.3a shows the UV-Vis-NIR spectra of the π plasmon peak for S1, S2 and S3 before and after centrifugation for 15 min and 60 min. The spectra in Fig. 3.4a are magnified 5 times relative to the corresponding spectra in Fig. 3.3, and as an example, the deconvoluted Lorentzians for S1, S2 and S3 centrifuged for 60 min is also shown. The most prominent peak in the spectrum at ~5.2 eV is attributed to the π plasmon mode along the radial direction. We observed another peak at ~4.5 eV which was previously attributed to the π plasmon mode along the nanotube axis by Murakami *et al.* [32]. As stated earlier,

different plasmon modes may couple due to tube-tube interactions in a SWNT bundle [28]. Hence, the free electrons behave like a 3D electron cloud and we expect to see a shift in the plasmon energy towards that of isolated SWNTs as the SWNTs are de-bundling. As stated earlier, in SWNTs the 1D Van Hove singularities near the Fermi energy are due to the energy dispersion near the K point of the Brillouin zone [27], whereas the π plasmon mode originates from the electronic excitations near the M point of the Brillouin zone [33].

Theoretical studies on the plasmon modes predict that the energy corresponding to the intra sub-band plasmon mode at the M point in an individual nanotube lies above that of bundled SWNTs [28]. In addition, the plasmon energy of SWNTs depends on the dielectric medium since the depolarization field (E_{dep}) arising from induced charges created at the interface (tube-tube or tube-medium interface), varies as a function of the dielectric constant [32]. An isolated SWNT in the suspension is completely surrounded by the solvent/surfactant medium. On the contrary, a SWNT in a bundle is screened from the solvent/surfactant medium by tube-tube interactions. Thus the π plasmon arising from π-π^* interband transitions at the M point is expected to vary with the bundle size due to dielectric screening and tube-tube interactions. To correlate the shift in the plasmon energy to the nanotube bundle size, we performed dynamic light scattering (DLS) studies on these samples.

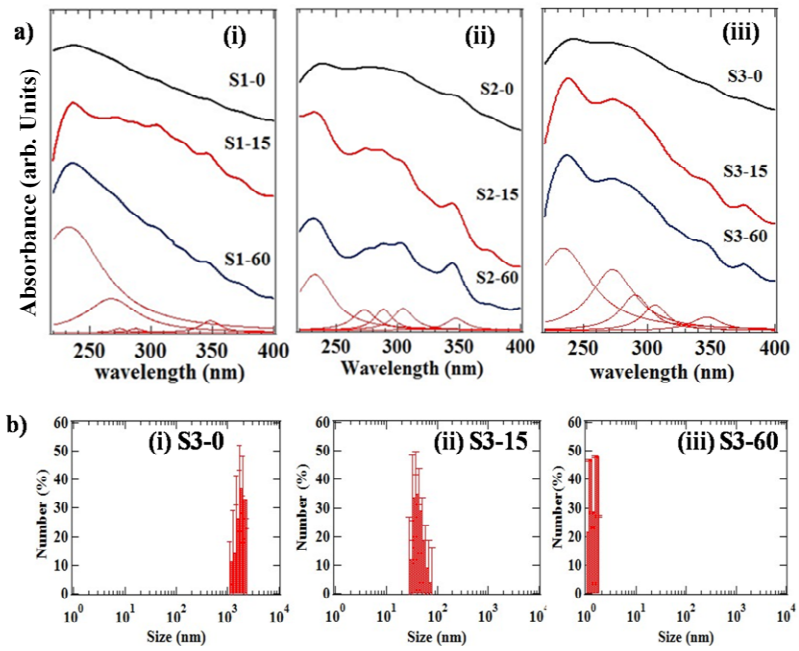

Figure 3.3: (a) UV–Vis–NIR spectra of (i) S1, (ii) S2 and (iii) S3 samples centrifuged for 60 min (blue), 15 min (red), and bundle samples (black). As an example, we show the deconvoluted Lorentzians (maroon) for S1, S2 and S3 centrifuged for 60 min. (b) Hydrodynamic size distribution of S3 for (i) as-grown bundled sample and samples centrifuged for (ii) 15 min and (iii) 60 min.

Dynamic Light Scattering

Dynamic light scattering (DLS) spectroscopy is an effective tool to study the diameter distribution of a sample in a solution. The typical setup for these measurements consists of a monochromatic laser source, a sample chamber and a detector connected to a signal processing device as shown in Figure 3.5. DLS measures the Brownian motion of the

particles in a solution and relates it to the size of the particle, the velocity of Brownian motion of particles is controlled by the translation diffusion coefficient of the liquid which depends on viscosity of the medium. In this process, incident light is scattered by the solution while the particles are under Brownian motion, this scattered light is collected by the detector and the rate at which the scattered light intensity changes as a function of time is calculated from the autocorrelation function. The autocorrelation function for the changes in intensities over a time t is given by

$$G_2(\tau) = < I(0)I(\tau) > = 1/T \int I(t) + I(t+\tau)dt \tag{3.2}$$

Where t is the time of scan and τ is the time difference. This value can be normalized to the first order autocorrelation function $G_1(\tau)$ using the equation

$$G_2(\tau) = 1 + \beta \left| G_1(\tau) \right|^2 \tag{3.3}$$

where β is an experimentally determined constant. If the particles are assumed to be spherical, then the first order autocorrelation function is given by

$$G_1(\tau) = e^{(-2q^2 D\tau)} \text{ and } q = \frac{4\pi n}{\lambda_0} \sin(\theta/2) \tag{3.4}$$

Where n, λ and θ are the refractive index, wavelength of incident light and the scattering angle respectively. The hydrodynamic size of the particles is determined using the Stokes-Einstein relation.

$$D = \frac{k_B T}{6\pi\eta D_h} \tag{3.5}$$

Where k_B is the Boltzmann's constant T is the temperature, D is diffusion constant and D_h is the hydrodynamic size

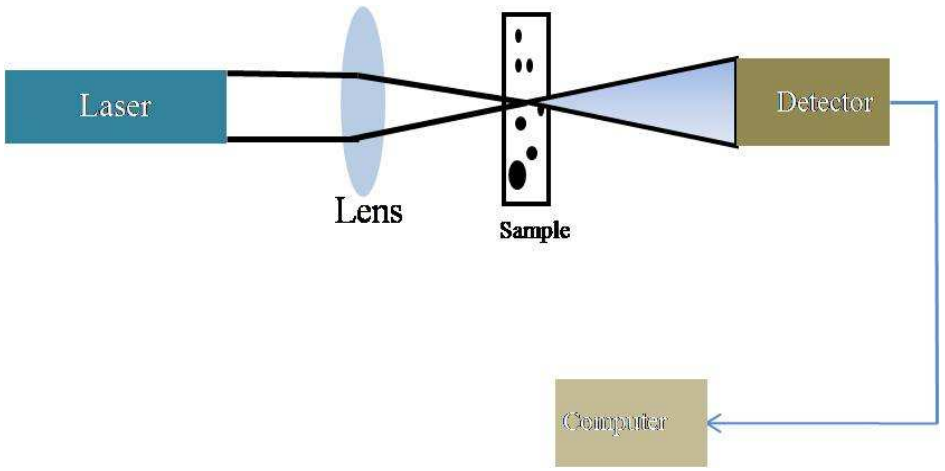

Figure 3.4: Schematic representation of the experimental setup for Dynamic Light Scattering spectroscopy.

Such DLS spectroscopic analyses were performed on our samples S1, S2 and S3. Figure 3.3b shows the hydrodynamic size distribution obtained for S3 at different centrifugation times. The mean bundle diameter is ~1850 nm for the bundled sample, and decreases to ~65 and ~1 nm after centrifuging for 15 and 60 min resulting from gradual de-bundling as well as precipitation of the SWNT bundles with increased centrifugation time. Although we have restricted our discussion to samples centrifuged at 15 and 60 min, similar measurements were done for S1, S2 and S3 at other centrifugation times (5, 30.

Sample	Centrifugation time (mins)	Hydrodynamic size (nm)	π plasmon peak position (nm)	π plasmon peak position (eV)
S1	0	491	237.5	5.21
	5	1.12	229.7	5.39
	15	1.11	230.4	5.38
	60	1.11	229.8	5.39
S2	0	1894	238.8	5.19
	5	135	236.7	5.24
	15	79	235.5	5.26
	30	1.15	232.7	5.33
	45	1.15	233.8	5.31
	60	1.14	232.4	5.33
S3	0	1846	239.4	5.18
	5	126	237.2	5.23
	15	64	237.6	5.22
	30	29	235.2	5.27
	45	1.42	233.9	5.31
	60	1.35	234.1	5.30
Carbolex	15	127	237.1	5.23
HipCo	15	61	235.8	5.26

Table 3.1. List of the SWNT hydrodynamic size and the π plasmon peak positions for S1, S2 and S3 as a function of centrifugation time. Similar data for commercially available Carbolex and HiPCo SWNT bundles are shown for centrifugation time of 15 min.

and 45 mins). Table 3.1 summarizes the bundle diameter of the samples at different centrifugation times along with the corresponding π plasmon energy values

Zeta Potential Studies

Zeta potential is a physical property exhibited by any particle that is in a suspension. The zeta potential value gives a measure of the stability of the solution. A layer of ions that are surrounding any charged particle in a suspension are strongly bonded. This layer is called Stern layer. The layer outside the Stern layer is called the diffuse layer, in which the ions are not as strongly bonded to the core. Within this diffuse layer, an imaginary boundary called the slipping plane exists, in which ions move with the particle when a voltage is applied but the ions outside this remain inert as shown in figure 3.5. The potential at such a boundary is called the Zeta potential.

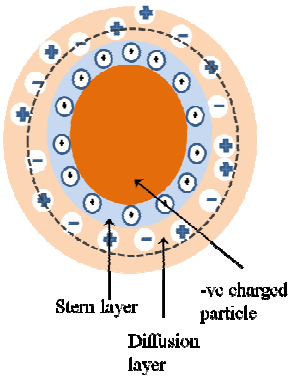

Figure 3.5: Schematic representation charge distribution around a negatively charged particle.

The Zeta potential values can be obtained from the mobility of the particles in a solution:

$$\mu = \frac{\zeta \varepsilon_m V}{4\pi\eta D}$$

Where μ is the mobility, ζ is the Zeta potential, V is the applied Voltage, ε_m, D and η correspond to the dielectric constant of the medium, electrode separation distance and the refractive index of the medium. The viscosity of the medium and mobility are related by $\boldsymbol{v = \mu E}$ where v is the drift velocity, E is the electric field and μ is the mobility.

Zeta potential measurements were performed on S1, S2 and S3 samples to quantify the degree of dispersion of sub-nm SWNTs in the solution. Table 3.2 lists the zeta potential (ζ) and mobility (μ) values for S1, S2 and S3 centrifuged for different times. The difference in the zeta potential values for the samples S1, S2 as S3 can be attributed to the difference in the diameter distribution of the samples. In general, when $|\zeta| > 15$ meV for a SWNT suspension, the SWNTs are considered to be highly dispersed. These high values of Zeta potential suggest a very high degree of stabilization of nanotubes due to the electrostatic repulsion between the layers of adsorbed surfactant molecules [34]. The negative zeta potential values obtained in our experiments are due to the anionic surfactant that coats the nanotubes.

Sample	Centrifugation time (min)	Zeta potential (meV)	Mobility (V/cm)
S1	0	-34.93	-2.73
	15	-22.86	-1.79
	60	-21.13	-1.65
S2	0	-40.37	-3.15
	15	-40.06	-3.13
	60	-38.93	-3.04
S3	0	-33.94	-2.65
	15	-41.81	-3.26
	60	-35.76	-2.79

Table 3.2: Zeta potential values for the samples centrifuged for different times.

As noted in Table 3.1, the π plasmon energies for S1, S2 and S3 vary from 5.17 to 5.3 eV. These values are in close agreement with the plasmon energy of 5.2 eV (for SWNT bundles with dominant tube diameter of 1.4 nm) reported by Pichler *et al*. using EELS. [21]. In Figure 3.6, we plot the plasmon energies listed in Table 1 to obtain an empirical relation between the shift in the π plasmon energy and the bundle diameter $D_{h.}$

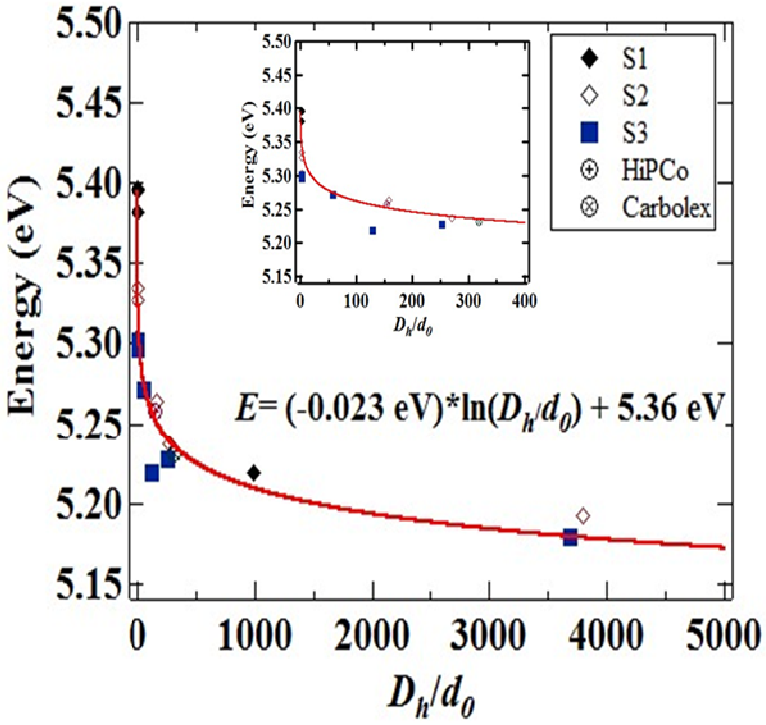

Figure 3.6: Plot of the π plasmon energy vs bundle diameter. Inset shows a similar plot for lower hydrodynamic size.

We find that the plasmon energy E can be expressed as E = (-0.023 eV)*ln(D_h/d_o) + 5.37 eV where d_o is the smallest tube diameter. The validity of this relation has been verified by studying the plasmon energy as a function of bundle size in Carbolex SWNTs (dominant dia. ~ 1.4 nm) and HiPCo SWNTs (dia. ~ 0.9 nm to 1.3 nm). We find that the results from these samples are in excellent agreement with the relation obtained in this study using sub-nm SWNTs. Rance *et al.* analyzed the dependence of the π plasmon energy on the diameter d of the nanotube ,but bundling/de-bundling affect on the π plasmon energy was ignored, which in this study are shown to be an important factor.

Conclusions

In summary, the π plasmon energy dependence on the bundle size in sub-nm SWNTs has been characterized using UV–Vis–NIR spectroscopy. DLS spectroscopy has been used to measure the hydrodynamic size of the SWNT bundle and the dispersion quality is obtained from Zeta potential measurements. For the first time, an empirical relationship has been observed between the plasmon energy and nanotube bundle diameter. This relation is consistent for Carbolex and HiPCo SWNTs. The observed shift in the π plasmon energy is consistent with the dielectric screening and symmetry lowering due to tube–tube interactions.

CHAPTER FOUR

EVIDENCE FOR EDGE STATE PHOTOLUMINESCENCE IN GRAPHENE QUANTUM DOTS

Introduction

Graphene has generated an enormous interest in carbon science and technology due to its unique properties [4, 35, 36]. Particularly, the high electron mobility (~10^6 cm^2 $V^{-1}s^{-1}$) of graphene is attractive for nanoelectronics [37, 38]. Several synthesis techniques have been reported to produce graphene [39]. Exfoliation of graphene from HOPG using scotch tape produces the purest form of graphene but it cannot be transferred onto the desired substrates for further use. Chemical vapor deposition technique has been widely employed to produce graphene on metal foils such as Cu, Ni Au and Pt [40-42], which can later be transferred onto desired substrates. For bulk production of grapahene, methods such as chemical exfoliation of graphite [43] and reduction of graphene oxide [44] are employed. However, graphene produced using these methods are of combination of a single, double and few layered graphene.

As discussed in chapter 1, the practical realization of graphene based logic devices has not yet been achieved due to the lack of a band gap in graphene. For any conventional graphene based logic applications, the dimensions of graphene must be below 100 nm to facilitate an opening of a band gap in its otherwise semi-metallic band structure [45-47]. To this end, several synthesis techniques have been developed over the past few years to

produce confined graphene structures such as graphene nanoribbons (GNRs) and graphene quantum dots (GQDs). GNRs can be fabricated using techniques such as unzipping of carbon nanotubes [48, 49], chemical vapor deposition [50] and other bottom up fabrication techniques [51]. More recently, researchers have produced graphene quantum dots using techniques such as hydrothermal or solvothermal reduction of graphene oxide [52, 53], microwave assisted technique [54], electrochemical methods [55] and other synthesis methods [56-58]. These GQDs show excellent photoluminescence properties and can potentially be used in the fields of drug delivery, bio-imaging, photovoltaic, *etc*. However, only a limited progress has been made towards fundamental understanding of the electronic and optical properties of GNRs and GQDs albeit their successful synthesis. Specifically, the origin of strong photoluminescence (PL) in GQDs , which has been attributed to the presence of emissive surface traps and.or edge states in GQDs, remains inconclusive to date.

Pan *et. al.* produced GQDs of mean diameter 10 nm using hydrothermal method. In their synthesis technique, graphene sheets were obtained from thermal reduction of graphene oxide pretreated with acids to create defects. The as obtained sheets were subjected to hydrothermal treatment and GQDs were obtained. The PL spectrum observed from these samples is broad and the emission peaks shift with the excitation wavelength. The origin of PL was tentatively attributed to the luminescent zig-zag edges, albeit experimental evidence to support this claim is still lacking. Other reports on GQDs claim that the size and the functional groups attached to these GQDs determine their PL behavior [53, 59].

However, a consensus regarding its origin is still lacking. Therefore, it is pertinent to probe the optical and luminescent properties of GQDs to elucidate the origin of PL. Based on a combination of synthesis, annealing and PL measurements of GQDs, carbon nano-onions (CNOs) and GNRs, we found the PL of GQDs to be independent of its suspension medium, and the edge states as the origin for observed PL in GQDs and GNRs. Furthermore, this study highlights PL signatures for a variety of carbon nanostructures and serves as a basis for further theoretical and experimental studies.

Experimental Section

GQDs used in the present study were synthesized using two simple methods: (i) a modified version of a previously reported solvothermal method [60], and (ii) a novel method using sonication techniques. In (i), ~200 mg of as-purchased graphene nanoplatelets (XG Science, grade-M, 8 μm wide and 5-8 nm thick) was mixed with 40 ml DMF (Alfa Aesar) and tip sonicated (power ~40 W) for 30 min before transferring the dispersion into a Teflon lined autoclave. The GQDs, hereafter referred as M1-DMF, were obtained following a heating step for 5 hrs at 200^0C and subsequent filtration through a 0.22 μm PTFE membrane. Another batch of GQDs (M1-NaOH) was prepared using an identical procedure in NaOH diluted in DI water (pH=9).

In (ii), the as-purchased graphene nanoplatelets were first hydroxylated at room temperature by mixing it with NaOH (in a weight ratio of 1:4) in ethanol. Next, the

solution was bath sonicated for 4 hours and filtered through a 0.4 μm polyamide membrane. The as-obtained powder was dispersed in DI water and filtered again. These filtration cycles were repeated until the pH was 7. The final product was heated to 80^0C for 24 hr to remove the residual moisture. ~100 mg of hydroxylated graphene nanoplateletes was dispersed in 40 ml DMF and tip sonicated for 3 hrs, followed with a filtration step through a 0.2 μm PTFE membrane. This sample is referred as M2-DMF. Another batch of GQDs (M2-NaOH) was prepared using an identical procedure in NaOH diluted in DI water (pH=9). The GQDs were characterized using a high resolution Hitachi TM 9500 transmission electron microscope (HR-TEM) which operated at 300 kV. A double grating Horiba Jobin Yvon spectrometer equipped with a liquid nitrogen cooled CCD was used for recording the room temperature PL data.

Annealing was performed in a quartz tube reactor; Sample wes loaded into the reactor, which was connected to a vacuum pump. The pressure inside the tube was slowly decreased using a needle valve until it reached ~1mbar. The reactor was then turned on to the desired temperature for 15 mins. After the reactor was cooled to room temperature, the GQD sample was re-dispersed in the solvent to perform further studies.

Results and Discussion

Figure 4.1a and 4.1c shows the transmission electron microscopy (TEM) image of as-obtained M1-DMF and M1-NaoH sample with a same mean diameter of ~ 4 nm. The

high resolution TEM (HR-TEM) image of an isolated GQD (Fig. 4.1b) and the Fast Fourier Transform (FFT) of the image is (inset in Fig. 4.1b) confirms the high crystallinity of the sample. The presence of a strong π– π* transition peak at ~4.5 eV (270 nm) in the UV-Visible spectrum (Fig. 4.2) further confirmed the sp^2 covalent bonding in our samples. This peak corresponds to the π plasmon mode which results from a π– π* transition at the *M* point in the Brillouin zone [61].

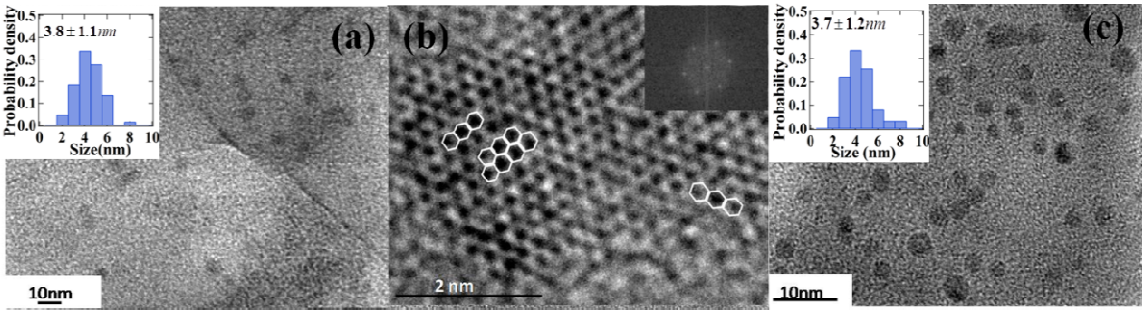

Figure 4.1: **(a)**TEM and (b) HR-TEM image of graphene quantum dots prepared using the solvothermal treatment in DMF, the zigzag edges are marked as a guide to the eye and the inset shows the FFT of the image in (b) and in (c) the TEM image of GQD prepared via the hydrothermal treatment in NaOH .The inset shows the diameter distribution of the corresponding samples

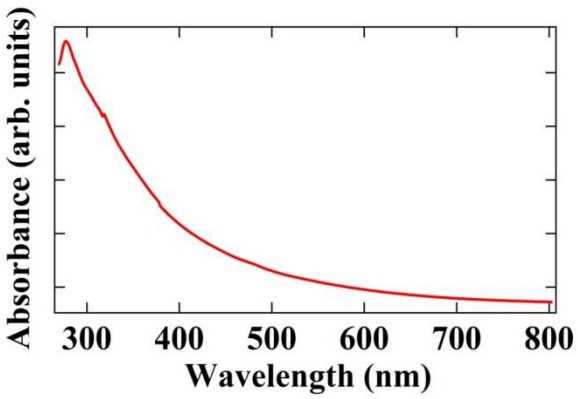

Figure 4.2: UV-Vis NIR spectrum of as synthesized graphene quantum dots suspended in ethanol.

The PL spectra for M1-DMF and M1-NaOH are very similar despite the difference in the solvents used in their synthesis (see Fig. 4.3). When excited at 400 nm, both samples exhibited green luminescence at ~510 nm with a broad FWHM of ~100 nm [57, 62, 63]. In fact, M1-DMF and M1-NaOH showed the same shifts (upshift up from 400-460 nm and negligible shift from 460-540 nm) in their peak emission wavelength with increasing excitation wavelengths. Although such shifts in the emission have been observed in GQDs and other nanocarbons, the underlying principle has not yet been identified conclusively. As shown in Fig. 4.5, a deconvolution of the GQD PL spectrum showed that the broad emission peaks are actually comprised of at least three distinct Lorentzians each with a FWHM of 40 +/- 10 nm. Clearly, the peak positions of the deconvoluted traces for M1-DMF (Fig. 4.5 a-c) and M1-NaOH (Fig. 4.5 d-f) are observed to be approximately the same. Hence, based upon the lack of any spectral differences between M1-DMF & M1-NaOH samples, we evidently rule out the possibility of surface

passivating functional groups or other surface emissive traps from the processing that bond to GQDs as the source for the observed PL.

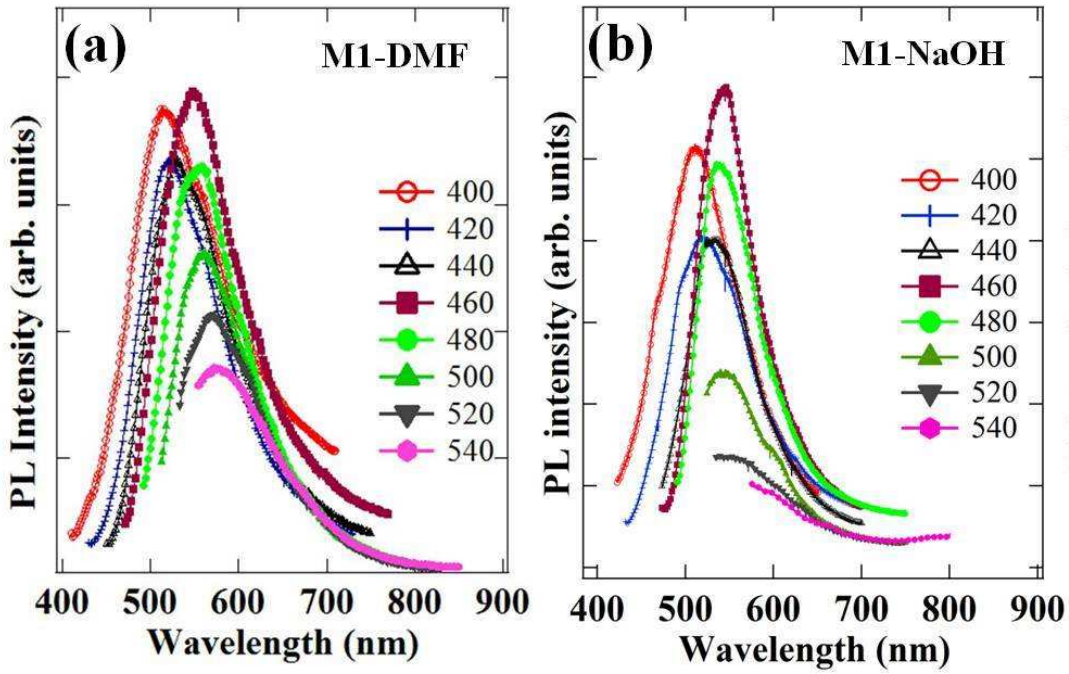

Figure 4.3: Photoluminescence spectra of graphene quantum dots as a function of excitation wavelength from 400 nm to 540 nm with 20 nm increments synthesize using solvothermal method in (a) DMF and (b) NaOH

Traditional semiconducting quantum dots of Si, CdSe, *etc.* [64, 65] are known to exhibit diameter dependent PL profiles due to a change in their band gaps as a function of diameter. Similar size dependence in GQDs was proposed by Eda *et. al.* [66] wherein the HUMO-LUMO gaps at the bonding and anti-bonding sites was proposed to change with

the size of GQD luminescence is size dependent. In order to address the effects of the size of the GQDs on the observed luminescence, we compare and contrast the PL behavior of GQDs synthesized using two different methods (solvothermal and ultrasonication) in the same solvent (DMF), viz., M1-DMF and M2-DMF. From the inset figures in Figs. 4.1a and 4.4a, the mean diameter of M2-DMF is slightly greater than that of M1-DMF. A closer look at their PL spectra (cf. Figs. 4.3a and 4.4c) reveal that at low excitation wavelengths their emission spectra differ slightly with an upshift in the emission wavelengths for M2-DMF. However, for higher excitation wavelengths from 440 nm to 540 nm, both M1-DMF and M2-DMF shows similar emission spectra. These characteristic changes are tentatively attributed to the change in the mean diameter of GQDs in M1-DMF and M2-DMF. As expected, the FWHM of the deconvoluted peaks for M2-DMF is ~40 nm (Figs 4.5g-i), consistent with the FWHM for M1-DMF and M1-NaOH. Interestingly, the M2-NaOH sample also showed a PL (Fig. 4.4d) behavior similar to that if M2-DMF sample despite the change in the solvent used. This result further supports our claim that the functional groups are not responsible for PL in GQDs. We further note that previous studies [52, 56, 60] on the PL of GQDs reported an upshift in emission wavelength by ~ 90 nm for increasing excitation wavelengths. The dependence of the three deconvoluted peak positions (labeled 1, 2 and 3 in Fig. 4.6a) on the excitation wavelength is significant for peak 1 as compared to peaks 2 and 3. In addition, a relative change in the intensities of these three peaks is evident with the second and third peaks becoming more prominent than the first peak with increasing

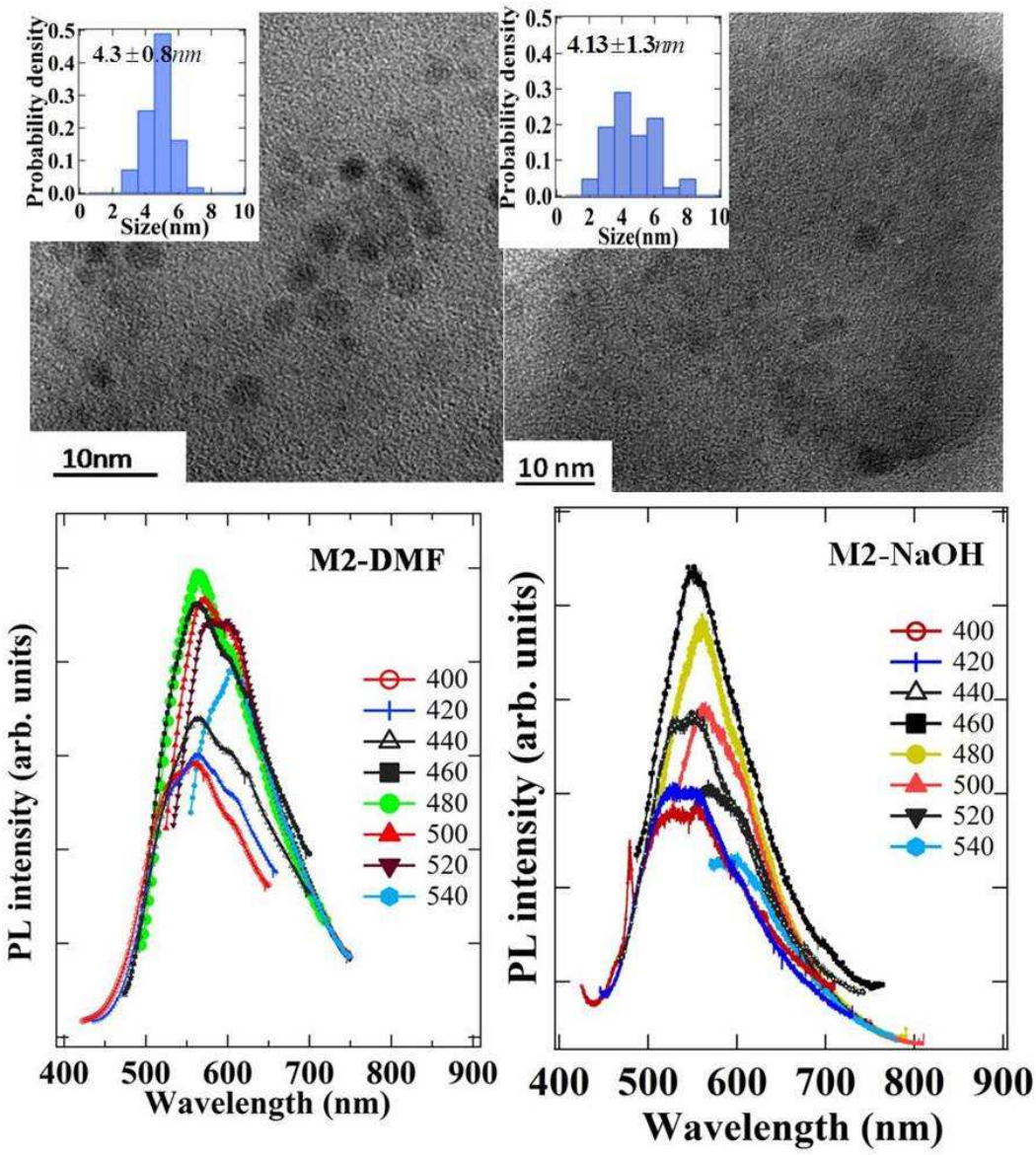

Figure 4.4**:** TEM images of graphene quantum dots prepared using the sonication treatment in (a) DMF and (b) NaOH solution, (c) and (d) represent their PL spectra.

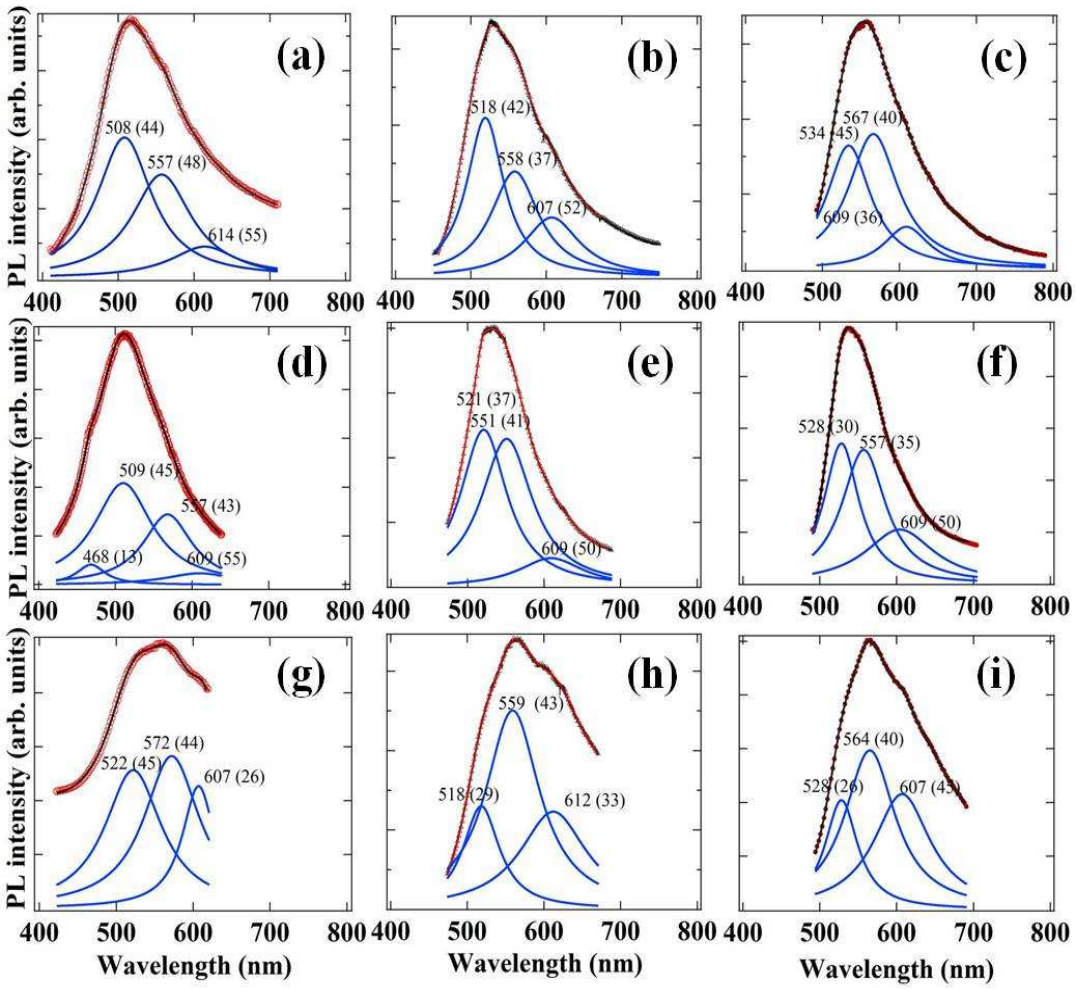

Figure 4.5: Deconvoluted fits corresponding to (a-c) M1-DMF, (d-f) M1-NaOH and (g-i) M2-DMF at 400 nm, 440 nm and 480 nm excitation respectively.

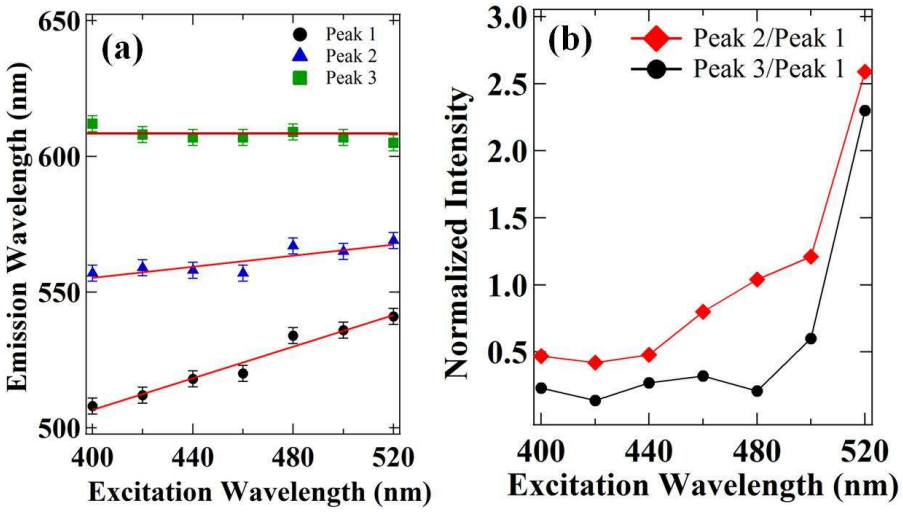

Figure 4.6: Plots of (a) emission peak positions of M1-DMF sample as a function of excitation wavelength and (b) the ratio of peak intensities with respect to peak 1.

excitation wavelength (Fig. 4.6b). These findings underscore the need for a detailed analysis (cf. Fig. 4.5 and Fig. 4.6) to ascertain the apparent ~90 nm shift in the emission wavelength reported in previous studies.

One of the important factors that might lead to the observed PL in GQDs is the presence of edge states. Previously, Pan *et al*. attributed the PL emission in GQDs to the triplet states from zig-zag edges. However, there is no experimental evidence yet to support this claim. In order to confirm the role of zig-zag edge states (proposed by Pan et al.) in the PL of GQDs, we vacuum annealed the M1-DMF sample and tracked the corresponding changes in its PL behavior when excited at 400 nm. Prior to the vacuum annealing step, the GQDs were harvested from the solution by evaporating the DMF. The as obtained

powder was annealed for 15 min at different temperatures under vacuum (~ 1 mbar) and the final products were re-dispersed in DMF for PL measurements. The presence of post-annealed GQDs was confirmed using TEM (see Fig. 4.8d). As shown in Figure 4.7, the PL spectrum of the M1-DMF sample, vacuum annealed at 250 ^{o}C for 15 min, exhibited a noticeable drop in the intensity of the PL signal.

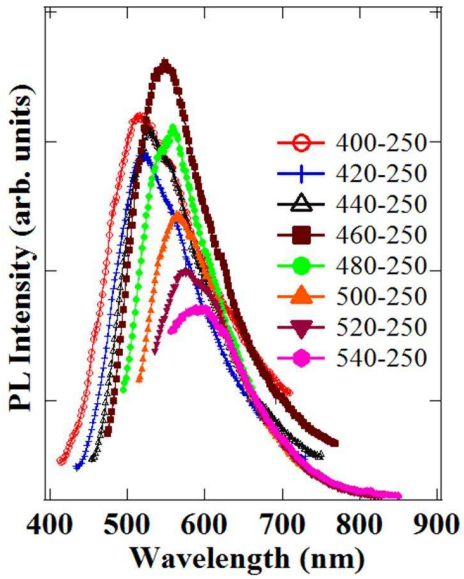

Figure 4.7: PL spectrum of M1-DMF sample annealed at 250^{o}C

Interestingly, the other spectral features such as the excitation dependent emission of the GQDs (cf. Fig. 4.3a) and the relative changes in the emission intensity as a function of excitation wavelength are identical to the as-prepared sample. Further, the PL intensity was observed to decrease with increasing annealing temperature. For comparison, we recorded the emission for the annealed GQDs using the 400 nm and 460 nm excitations

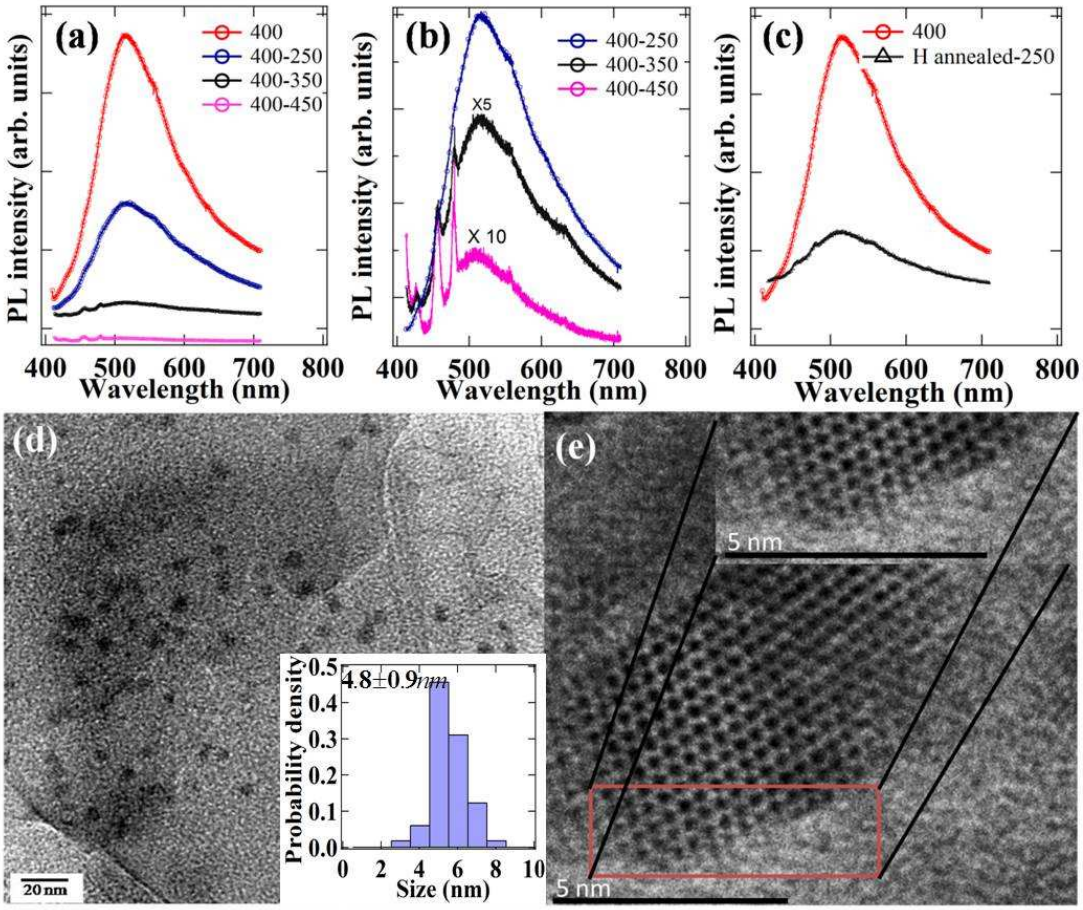

Figure 4.8: a) shows the change in the intensity of PL emission with 400 nm excitation as a function of annealing temperature, (b) shows the magnified view of the PL spectra of annealed samples, the sharp features correspond to the overtones of the excited light, (c) shows the change in the intensity of PL emission with 400 nm excitation upon annealing in hydrogen atmosphere,(d) TEM image and (e) HRTEM image of GQDs post annealing at 450^{o}C, atomic resolution which confirms the graphitic nature of the GQDs after annealing (inset shows the presence of disordered edges in GQDs)

and found a decrease in the PL intensity with increasing annealing temperatures (Fig. 4.8a and 4.9a).

We attribute this reduction in PL intensity to the possible rearrangement/passivation of edge carbon atoms in the GQD. Previous work done by Xu et. al. suggested that graphene edges tend to reconstruct upon annealing in vacuum [67]. However, the former argument can be ruled out due to the fact that the as-prepared sample has armchair, zigzag and disordered edges, and since it is structurally impossible for the circumference of the GQDs to have same family of edges (either armchair or zigzag), it is obvious that after annealing the sample would still have mixed edges, although perhaps in different ratios. The evidence for the presence of disordered edges can be seen from the HR-TEM images of a single quantum dot before (fig 4.1b) and after annealing (fig 4.8e). Thus, the rearrangement of edges is essentially random and does not result in a preferred chirality (armchair or zigzag). Hence, the possibility of zig-zag edges leading to the PL of GQDs may be eliminated.

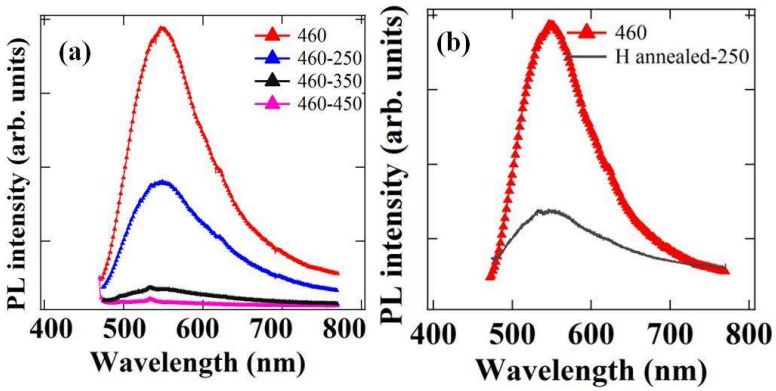

Figure 4.9: (a) shows the change in the intensity of PL emission with 460 nm excitation as a function of annealing temperature and (b) shows the change in the intensity of PL emission with 460 nm excitation upon annealing in hydrogen atmosphere.

It is important to note that the possibility of chiral edge luminescence cannot be ruled out based on the vacuum annealing experiments, however. In view of our experiments, it is incorrect to attribute the origin of PL to one family of edges. In a detailed theoretical modeling done by Radovic et. al. [68], they proposed that the armchair and zigzag edges would behave like carbene and carbyne sites respectively and an electronic excitation from HOMO-LUMO levels is possible irrespective of the chirality. On the other hand, the diameter distribution of the annealed sample is ~ 4.8 nm, slightly higher than the as-prepared sample. This slight shift in the diameter can be attributed to the agglomeration of GQDs during annealing and it should be noted that this shift in the diameter did not account for any new features in the PL spectrum.

In order to validate the passivation-induced reduction in the PL of GQDs, we had annealed the M1-DMF samples in an H_2 atmosphere (rather than vacuum) at lower temperatures (250^{o}C). Interestingly, the PL was quenched upon H_2 treatment (Fig. 4.8c and 4.9b) suggesting that the edge passivation indeed lowers PL intensity. Similar annealing experiments performed on M2-NaOH sample also showed a drop in the PL intensity analogous to M1-DMF samples (Fig. 4.10). This further validates that the PL signal is solely due to the presence of free edges irrespective of the synthesis techniques and solvents used. Although annealing experiments in this study suggests edge passivation in GQDs from residual solvent or surrounding atmosphere, an analytical evidence for this mechanism is lacking. To gain insight into the edge passivation process, FTIR spectroscopy has to be performed on the samples.

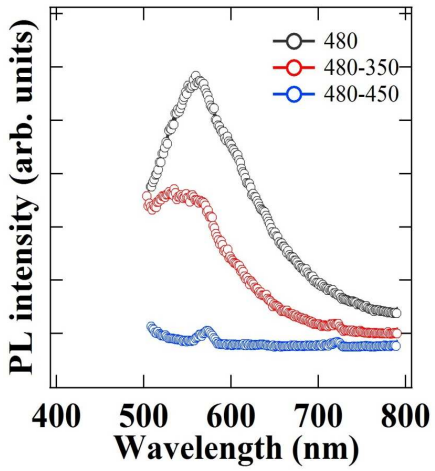

Figure 4.10**:** shows the change in the intensity of PL emission with 400 nm excitation as a function of annealing temperature for M2-NaOH sample.

To further confirm this hypothesis, we performed PL studies on few-layer GNRs with a uniform width of ~25 nm and length ~200 nm (inset in Fig. 4.11a). The PL spectrum of GNRs was strikingly similar to that of the GQDs with a nearly identical excitation-dependent emission profile (Fig. 4.11b). The similarity in the PL spectra of GQDs and GNRs, despite the differences in their morphology and size, confirmed that the PL indeed originated from the disordered edge states. It should be noted that the sharp peaks observed in the PL spectrum of GNRs are due to the overtone modes of the excitation wavelength and occurs at an interval of $\lambda/8$ where λ is the excitation wavelength.

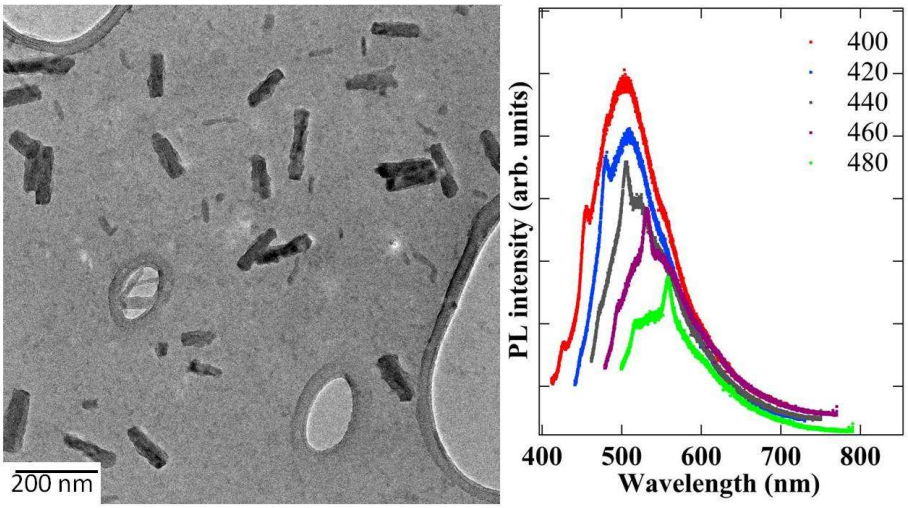

Figure 4.11: (a) TEM image and (b) PL spectra of GNRs

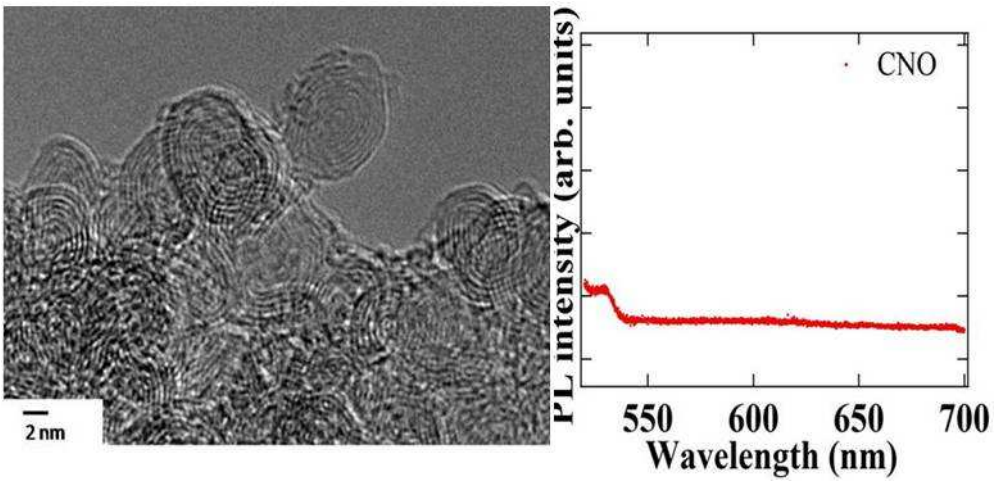

Figure 4.12: (a) TEM image and (b) PL spectra of CNOs

Along with GQDs and GNRs, we extended our PL studies to other forms of carbon systems such as carbon nano onions (CNOs). CNOs are a cage like structures formed with concentric buckyballs wrapped on top of each other, they consist of a combination of hexagonal and pentagonal arrangement of carbon atoms. It is important to note that there are no free edges in CNOs due to their closed cage-like structure. As expected, we did not observe any PL signal for CNOs (Fig. 4.12b) in agreement with the edge-state hypothesis. These results provide strong evidence that the edges are responsible for the luminescence in carbon systems.

Photoluminescence in Poly-aromatic molecules

The PL mechanism in GQDs can be well understood by studying the luminescence behavior in poly aromatic hydrocarbons. Benzene (C_6H_6) with six carbon and six hydrogen atoms forms the basis for the structure of aromatic compounds. The degree of conjugation and the arrangement of these benzene rings leads to different type of aromatic molecules such as napthalene, anthracene, pyrene, phenanatracene, pentacene etc,. Their structures are shown in figure 4.13. All these compounds have in-plane σ bonds and out of plane π bonds similar to graphene, the σ bonds are stationary where as the electrons in the π orbital forms delocalized state above and below the σ bonds. Based on the standard quantum confinement model, this spreading out of the wave function leads to a reduction in the energy [14], So, as the degree of conjugation of benzene rings is sincreased, the confinement energy is reduced. This means that the absorption and emission spectra shifts to higher wavelength or lower energies with an increase in the size of the molecule.

To understand the absorption and emission process in these molecules, an understanding of the energy level diagram is important. Unlike the case of 2D materials where the energy levels are continuous, the electronic states in these molecular systems are quite discrete. Based on the spin multiplicity, the exited states can be classified into singlet and triplet states. Since a transition from the ground state to an exited triplet state is forbidden by selection rules, an optical absorption always takes place between singlet levels.

However, during the decay process, an electron can take several available path ways depending on the energy gap between the adjacent levels as explained in chapter 2. These absorption and emission processes for aromatic molecules generally occur in ultra violet and visible regions.

Figure 4.13 shows the emission spectrum of different aromatic compounds and it is clearly seen that the emission spectrum red shifts with an increases in the benzene rings. It should be noted that in case of benzene, naphthalene and pyrene, the spectrum is recorded in cyclohexane solution where-as DMF is used for anthracene. So, the slight red shift in the anthracene spectrum can be attributed to the solvent effects. From these observations, we show that GQDs may be viewed as a highly conjugated system of benzene rings with its emission peaks (peak1, peak 2 and peak 3 in Fig. 4.6) arising from HOMO-LUMO levels similar to that of poly-aromatic molecules. Further theoretical studies are needed to gain better understanding of PL behavior in GQDs. An analytical model controlling the aromticity of GQDs by hydroxylation may serve as a good starting point to understand the role of conjugation on the PL spectrum of GQDs.

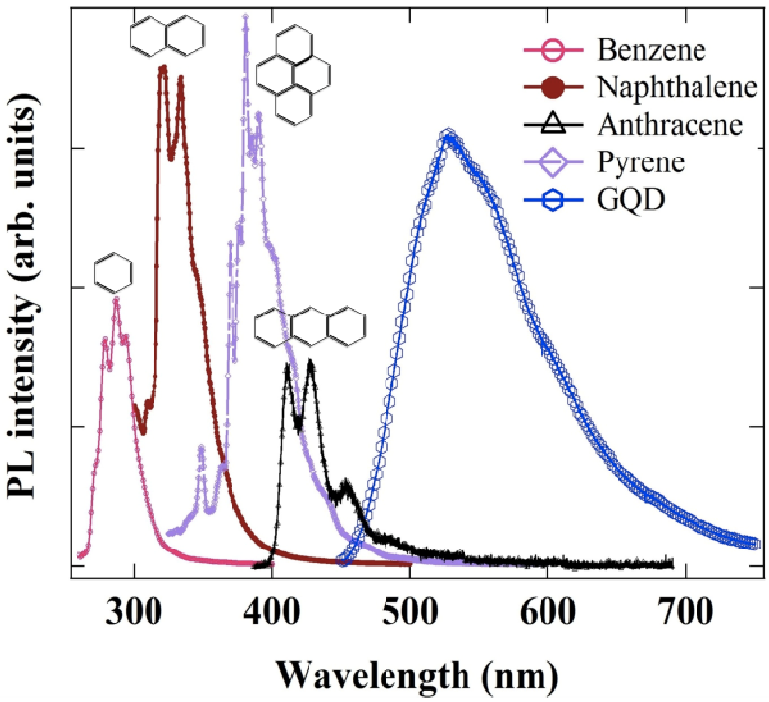

Figure 4.13: PL emission spectra of Benzene*, naphthalene*, Pyrene* in cyclohexane solution and Anthracene and GQDs in DMF. (* Raw data for these molecules is obtained from http://omlc.ogi.edu/spectra/PhotochemCAD/).

Conclusions

In summary, we performed an in-depth study of the PL emission properties of GQDs. Specifically, the origin of strong photoluminescence (PL) in GQDs, based on experiments in two different solvents, we have ruled out the possibility of surface passivating functional groups, or other surface emissive traps bonded to GQDs, as the source for the observed PL in GQDs. Based on a combination of synthesis, annealing and

PL measurements of GQDs, carbon nano-onions (CNOs) and GNRs, we found disordered edge states as the origin for observed PL in GQDs and GNRs. Lastly, we attribute the emission peaks to the its emission peaks arising from HOMO-LUMO levels similar to that of poly-aromatic molecules. Furthermore, this study highlights PL signatures for a variety of carbon nanostructures and serves as a basis for further theoretical and experimental studies.

CHAPTER FIVE

REEXAMINATION OF INFRARED SPECRA OF BISMUTH NANORODS: L-T TRANSITION OR EXTRENSIC PHASES

Introduction

Since the 1960s, the Fermi surface topology of bismuth (Bi) has been a subject of extensive theoretical and experimental study [69-72]. In general, Bi adopts a rhombohedral crystal structure that can also be treated as a slightly distorted cubic structure. This distortion gives rise to a very small overlap between electron ellipsoids (at the *L* points of the Brillouin zone (BZ)) and a hole ellipsoid (at the *T* point of the BZ), leading to a compensated semimetal that has small and equal population of electrons and holes at all temperatures as shown in Figure 5.1. The Fermi surface of Bi thus has three *L*- point electron pockets and a *T*-point hole pocket. The volume of each ellipsoidal pocket is only 10^{-5} of the BZ. This tiny, but finite Fermi surface profoundly impacts the electrical and optical properties of Bi in the following ways: (*i*) the occupancy of the electron and hole bands in the vicinity of the Fermi level is very sensitive to temperature because of anisotropic thermal expansion as well as thermal broadening of the Fermi distribution; (*ii*) the electron-phonon coupling is weak because the sub-thermal phonons to which the charge carriers are coupled are fewer; and (*iii*) the Fermi wavelength is large and hence the electron-point defect scattering is weak.

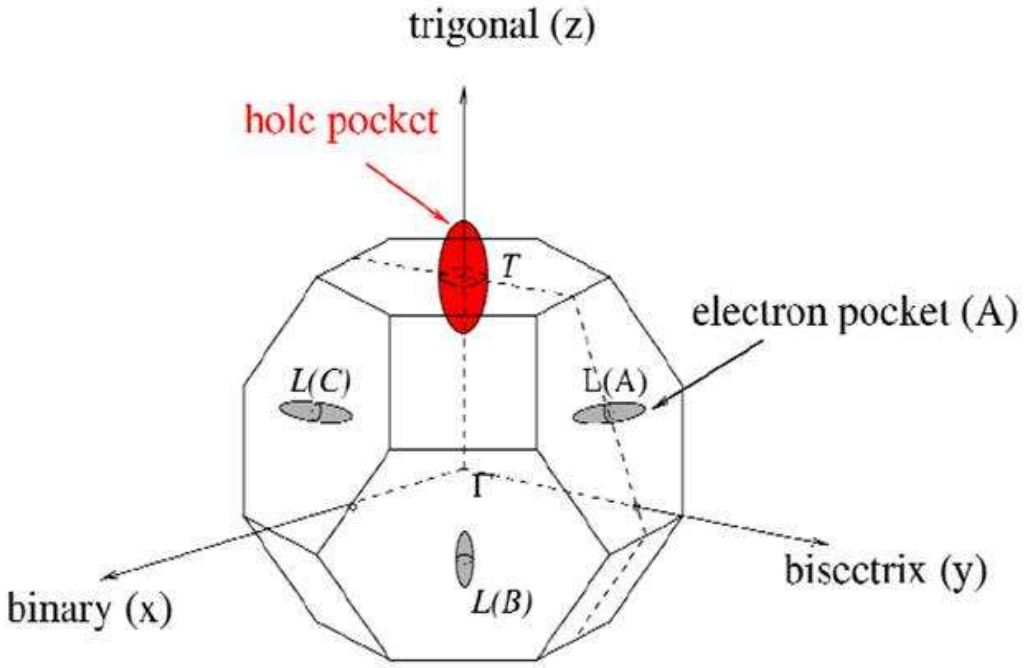

Figure 5.1: The Brillouin zone of Bi showing three *L* point electron pockets and one *T* point hole pocket [73]

The last two features lead not only to an exceptionally long electron mean free path in large, pure samples, but also allow observation of classical and quantum size effects at a larger length scale and at higher temperatures than most of the other materials. For example, a semimetal to semiconductor transition upon decreasing the diameter lower than ~ 50 nm [74] was first theoretically predicted and later confirmed in Bi nanowires, helping to initiate a new paradigm of nanostructured thermoelectrics. The transport properties and quantum confinement effects in Bi have been extensively studied [75, 76].

While these quantum confinement effects are useful for developing novel optical and electro-optical devices, optical measurements such as infrared (IR) spectroscopy are sensitive probes for monitoring changes in the quantum confinement induced Fermi surface topology.

Another noteworthy property of Bi is its surface states. Along these lines, spin-orbit-split surface states have been observed in Bi (001) ultrathin films using angle resolved photoemission spectroscopy (ARPES) [77]. On the surface of bulk Bi, the strong spin-orbit coupling along with the unusual Fermi surface topology give rise to a robust gapless excitation spectrum at the surface and on the edges of the crystal. These gapless excited states form what has been called a "topological metal", and are a prerequisite for the formation of topological insulators [78, 79]. In fact, surface states in clean cleaved semi-infinite Bi surfaces have been found to show high electron densities and large spin-orbit splitting due to the loss of inversion symmetry (i.e., Rashba effect) [80, 81].

Spectroscopic analysis of quantum effects in Bi nanostructures is a challenging task due to the factors mentioned above, such as the strong size and temperature dependence of the Fermi surface topology, the existence of surface states and the presence of native oxides and carbides in Bi. In this review, we re-examine the Fourier transform infrared (FTIR) spectra of Bi nanorods with an emphasis on the physical origin of the IR peaks

that have been previously attributed to the *L*-*T* transition. The article is organized as follows. First, we briefly review the existing theoretical models describing the size dependence of the *L*-*T* transition and the relevant synthesis efforts of Bi nanostructures (section 2). Then we discuss the theoretical model describing the temperature dependence on the IR spectra of the Bi nanorods, followed by experimental results. Finally we compare the experimental spectra of micro and nanostructures of Bi with the theoretical predictions described in section 2 as well as with the properties of bulk Bi.

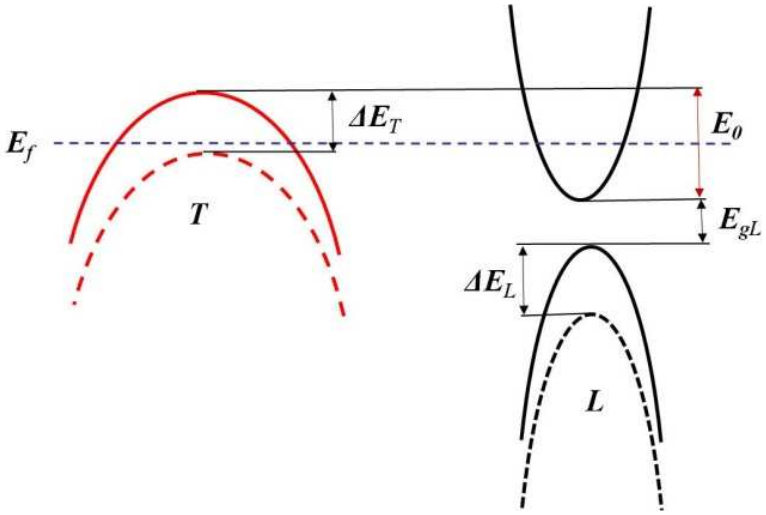

Figure 5.2: A schematic of the Bi band structure at room temperature near the Fermi level as the nanowire diameter decreases. E_{gL} is the direct band energy gap at the *L*-point, E_0 is the band overlap between the holes at the *T*-point and electron at the *L*-point, ΔE_L and ΔE_T are the energy differences with respect to the band edges at the *L* point and at the *T* point respectively.

Size Dependence of the *L-T* Transition

Theoretical model

The optical properties of Bi are intimately related to the size and temperature of its Fermi surface topology. As discussed above, the Fermi surface of Bi has very small ellipsoidal electron carrier pockets centered at the *L* points and a small hole pocket centered at the *T* point along the axis of 3 fold symmetry fig. 5.1) [82].

For bulk Bi, the conduction and valence bands at the *L* point are separated by a small direct energy gap (E_{gL} = 13.8 meV), and are non-parabolic as shown in Fig. 5.2. Meanwhile, there is a small overlap E_0 = 38 meV between the electron states at the *L* point and the hole states at the *T* point. These values hold true for up to ~ 80 K above which the temperature dependence becomes important. At room temperature, the *L* point band gap E_{gL} is estimated to be 36 meV with a band overlap E_0 of 98 meV [83-85] .This band overlap is predicted to diminish, disappear and end up with a small indirect gap as the diameter of a Bi nanowire decreases below ~ 50 nm and the sub-band spacing increases. Since the *L* point effective mass is smaller than that of the *T* point, the *L* point valence band edge will decrease faster than the *T* point valence band edge. As a result, the indirect *L-T* transition energy, $E_{L\text{-}T}$, should increase as the diameter of the nanowires decreases (Fig. 5.2) [83].

It is important to note that electrons in a 1D nanowire are confined along the direction in the plane normal to the wire axis (i.e., "in-plane"), and hence their momentum normal to the wire axis is quantized. The size dependence of the *L-T* transition energy is further given by [74]:

$$E_{L-T} \approx \frac{\hbar^2 \pi^2}{m^* d^2} \tag{5.1}$$

Where m^* is the in-plane effective mass ($0.001m_0$ to $0.26m_0$, depending on the direction), m_0 is the free electron mass, d the diameter of the nanorod and $\hbar$ the reduced Planck's constant. This *L-T* transition (E_{L-T}) should be experimentally observable in the infrared region and can be tracked as a function of nanowire diameter (d). Levin *et al.* [83] modeled a relation for the energy threshold of the *L-T* transition

$$E_{L-T} = E_{gL} + E_0 - \Delta E_L(d) + \Delta E_T(d) \tag{5.2}$$

where $\Delta E_L(d)$ and $\Delta E_T(d)$ are the energy differences with respect to the band edges at the *L* point and at the *T* point, induced by the size effects. This is the effect that has been proposed to cause the size dependence of the IR peaks in Bi.

Synthesis of Bi nanostructures

Motivated by these theoretical works, several groups have synthesized various forms of Bi nanostructures such as nanoparticles, nanotubes and nanorods. Li *et al.* synthesized Bi nanotubes of diameter ~5nm using a low temperature hydrothermal method [86].

Derrouiche*et al.* synthesized Bi nanotubes using solvothermal synthesis and chemical reduction methods [87]. Recently, Shim *et al.* synthesized Bi nanorods of larger diameter (> 100 nm) using a novel technique called the ON-OFF method [88]. In this process, Bi thin film is deposited on a thermally oxidized Si wafer which is loaded into a vacuum furnace for thermal annealing. During the annealing process, stress is induced inside the Bi film due to the difference in thermal expansion of Bi and the substrate which leads to the formation of nanowires [88]. Lee *et al.* modified the ON-OFF method and obtained Bi nanorods of diameter < 100 nm. They observed a semimetal to semiconductor transition in Bi nanorods of diameter 63 nm, 58 nm and 42 nm from the transport measurements conducted on individual wires [89]. Several other groups also observed evidence consistent with this indirect *L-T* transition in Bi nanorods through measurements of temperature and magnetic field dependencies of the electrical resistance [75, 90] and room temperature IR studies [82, 84, 91]. Wang *et al.* [92] have confirmed the semimetal-to-semiconductor transition in 5-500 nm diameter Bi nanoparticles prepared by reducing Bi^{3+} with sodium borohydride in the presence of poly-vinylpyrrolidone. Rogacheva *et al.* [93] observed a semimetal to semiconductor transition in Bi thin films when they measured the temperature dependences of the Hall coefficient and established that a film thickness smaller than ~25–30 nm exhibited no semimetallic conductivity.

Another widely used method to fabricate Bi nanostructures is the template assisted synthesis technique. In this method, Aluminum (Al) is anodized using various acids to

fabricate pores of the desired diameter. The size of the pore depends on the anodizing conditions used in the experiment and the resulting oxide film possesses highly ordered, cylindrical channels that favor the growth of nanorods [94-96]. For Bi nanowires synthesis, the porous film was placed inside a high pressure reaction chamber and high purity Bi pieces were placed around the porous film. As the temperature of the reactor is raised to the melting point of Bi (271^0C), the Bi pieces melt and due to the high pressure created inside the reactor, molten Bi is driven into the pores of the template forming nanorods inside the template [90, 97]. The optical absorption studies conducted by Black *et. al.* on these samples showed infrared peaks at 965 cm^{-1} and 1090 cm^{-1} for samples with average diameter of 200 nm and ~ 45 nm respectively (Fig. 5.3) [91] and the orientation of these nanorods was determined to be along the $[01\bar{1}2]$ crystalline direction. Black *et al.* attributed this energy feature to the indirect *L-T* transition. These results indicated that the energy corresponding to the indirect interband transition increased with the decreasing nanowire diameter which is in good agreement with theoretical predictions.

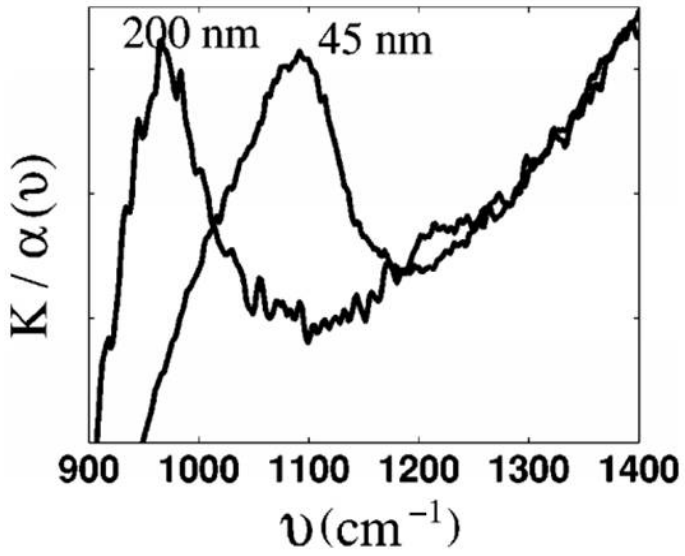

Figure 5.3: FTIR spectra of Bi nanowires of diameter 200 nm and 45 nm showing peaks at 965 cm^{-1} and 1090 cm^{-1} respectively. K is the imaginary part of index of refraction and α is the absorption coefficient [91].

However, it is important to note that not all experimental results support the scenario of the *L-T* transition. Huber *et al*.[98] measured Shubnikov-de Hass (SdH) magnetoresistance measurements on 80 nm and 30 nm Bi nanorods arrays prepared by the template method. They found that the SdH measurements on 80 nm nanorods showed a reduced hole carrier density. These results are consistent with the proposed semimetal to semiconductor transition. Surprisingly, they found that the Fermi surface in 30 nm nanorods is nearly spherical and has a large charge density and relatively large effective

mass. These results questioned the existing theoretical *L-T* model. The high carrier density has been attributed to surface-induced charge carriers.

Following the work done by Black *et. al.*, we synthesized Bi nanorods of diameter ~10-25 nm using the pulsed laser deposition (PLD) technique (Fig. 5.4a) [99]. This method is based on a vapor-liquid-solid growth process. In a typical synthesis, a Bi target impregnated with 1 at. % Au, is mounted on a rotating rod and placed inside a quartz tube. The target is ablated with a Nd:YAG laser (1064 nm excitation and 650 mJ/pulse, 10 Hz) while the temperature of the quartz tube is maintained at 200 ^{O}C, Ar and H_2 are used as carrier gases. As the target is ablated, the vaporized material flows downstream and condenses on a cold finger.

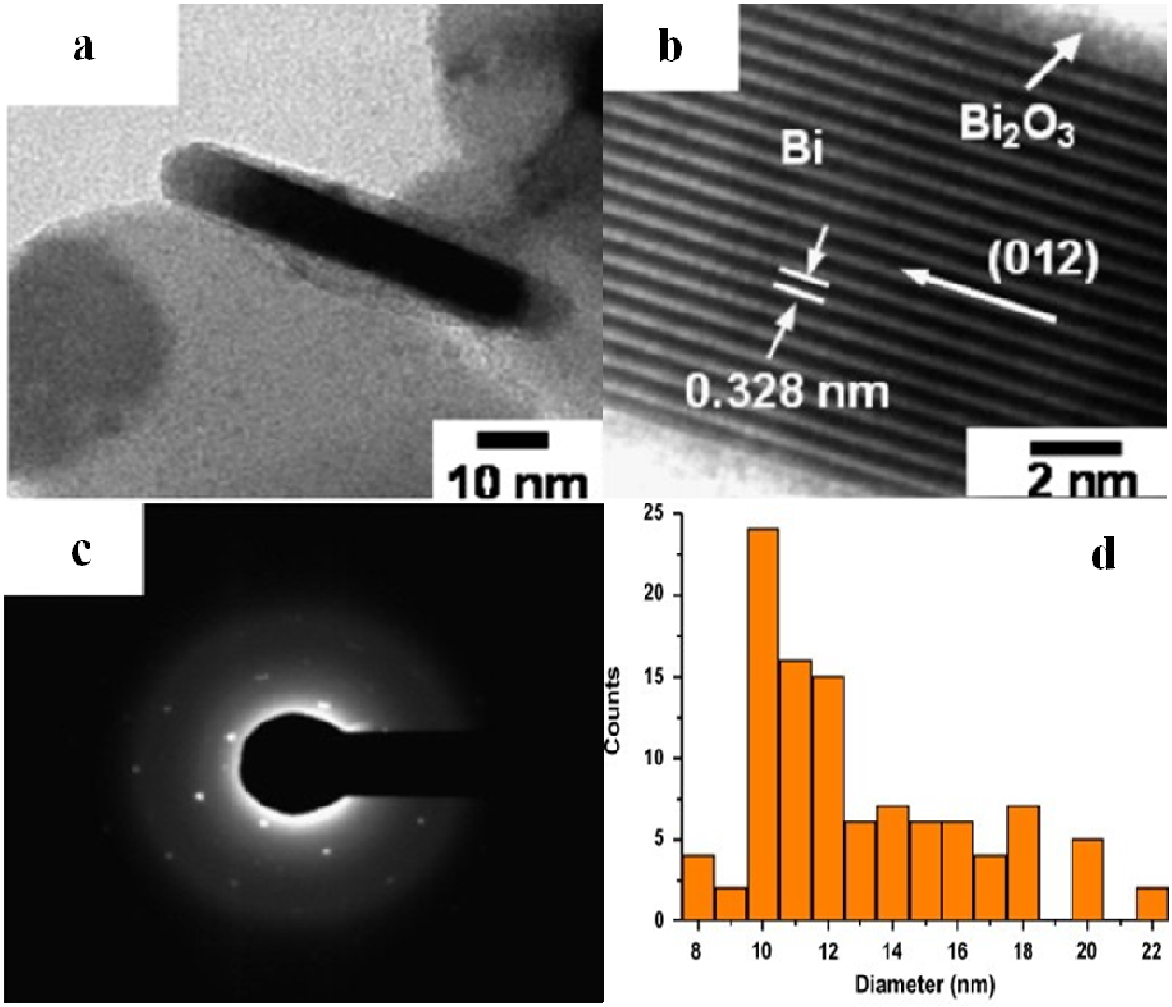

Figure 5.4: (a) HR-TEM image of an isolated Bi nanorod (diameter of ~10 nm) with its thin native oxide layer. (b) HR-TEM image of a Bi nanorod showing the excellent ordering of the lattice planes. (c) Selected area diffraction pattern of Bi nanorods, and (d) Diameter distribution of as-prepared Binanorods. Adapted from Ref. [99].

High Resolution Transmission Electron Microscopy (HR-TEM) analysis on the as-synthesized Bi nanorods showed excellent ordering of lattice planes with a lattice spacing of 0.328 nm (Fig. 5.4b). Selected area diffraction pattern showed the growth direction to be along the $[0\,1\,\bar{1}\,2]$ crystalline direction (Fig. 5.4c). The thin layer (~ 2nm) surrounding the nanorods has been attributed to the oxide phase of Bi (Fig. 5.4b) [99]. Figure 5.4d shows the diameter distribution of these nanorods with a peak around 10 nm. In this article we focus our discussion on the IR spectra of Bi nanorods synthesized using porous alumina templates by Black *et al.* [91] and Bi nanorods synthesized using the PLD technique [99].

Room temperature FTIR spectra of our as-synthesized Bi nanorods showed the presence of an intense peak at 1393 cm^{-1} which was attributed to the indirect *L*-*T* transition (Fig. 5.5). A second peak was also present at 1460 cm^{-1}. This second peak was attributed to an indirect process in the scheme of Black *et al.* [82, 91] in which the incident photon generates a phonon spanning the *L* and *T* points in the Brillouin zone, providing for momentum conservation, as well as a photon of energy of 1393 cm^{-1} to excite an electron from the *L* point valence band to the *T* point valence band. An additional third absorption peak was seen as a weak shoulder around 1355 cm^{-1} and was attributed to the absorption of a phonon spanning the *L* and *T* points and the excitation of an electron from *L* to *T* points in the Brillouin zone [89]. Furthermore, given the broad diameter distribution of the nanorods in the synthesis process, one would expect broad peaks.

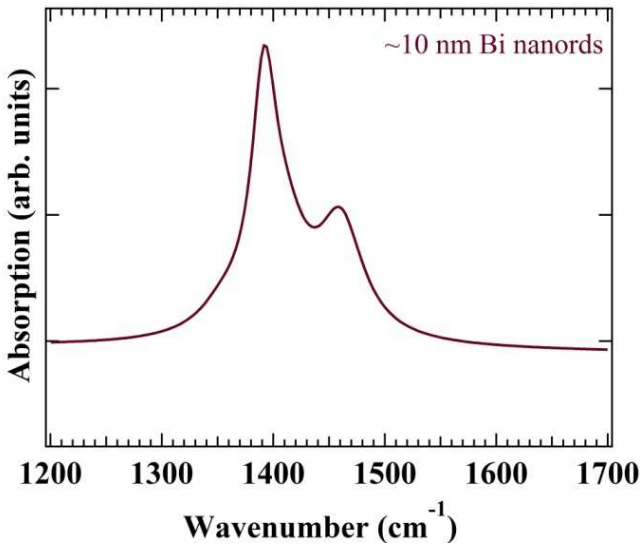

Figure 5.5: Room temperature FTIR spectrum of ~ 10 nm Bi nanorods [[99]].

Levin *et al.* [83] calculated the in-plane effective mass at the *T* point and at three *L* points for nanorods along a given orientation and plotted the energy $E_{L\text{-}T}$ as a function of $1/d^2$ (Fig. 5. 6) for the parameters of the non-parabolic model where $E_{L\text{-}T}$ is given by

$$E_{L-T}(d) = E_{gL} + E_0 - \frac{E_{gL}}{2} * \left(1 - \sqrt{1 + \frac{1}{E_{gL}} \frac{h^2}{m^*_{L,p} m_0 d^2}}\right) - \frac{h^2}{4 m^*_{T,p} d^2} \qquad (5.3)$$

Where $m^*_{L,p}$ and $m^*_{T,p}$ correspond to the effective mass of L and T pocket respectively. Levin *et. al.* included all three experimental data points (Black *et al*. [91] (Fig. 5.3) and 10 nm diameter nanorods [99] (Fig. 5.5) and concluded that the experimental results best fit the *L(C)-T* electronic transition (Fig. 5.6).

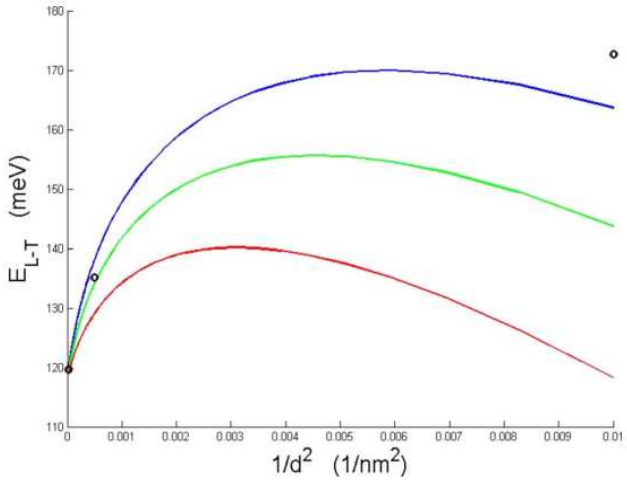

Figure 5.6: Plot of E_{L-T} vs *1/d2* for non parabolic model with *d* ranging from 10 to 300 nm. The three experimental data points are shown in open circles and they best fit to L(C)-T transition[83]

Temperature dependent IR studies

The size-dependent experimental results discussed above appear to be consistent with the model of the *L-T* transition, however, the temperature dependence of the *L-T* transition was largely ignored in the above mentioned studies. Using the empirical relationship determined for the temperature dependence of the band parameters associated with electron pockets [85] (table 1), we have expanded on the non-parabolic model presented by Levin *et al.* [83] (equation 3) to predict the energy of the indirect *L-T* transition for a range of temperatures (from room temperature down to 100 K). This non-parabolic

model of the *L*-*T* transition implies strong temperature dependence. The *L* point band structure, in contrast to the *T* point, has strong temperature dependence above 80 K due to the coupling between the non-parabolic *L* point valence and conduction bands.

We derived the $E_{L\text{-}T}$ transition using the *L(C)* effective mass components, as a function of temperature. As seen in Fig. 5.7a, for the *L(C)*-*T* transition, we would expect to observe a downshift of the transition frequency on the order of ~240 cm^{-1} (in the IR absorption spectrum) for nanorods with diameter ~10 nm as the temperature decreases from 300 K to 100 K. We would also expect a narrowing of the peaks, as the lower temperatures should reduce the dissipation. Although the values used for the bulk band parameters are not known with high accuracy at these temperatures, the temperature-induced shift in frequency should still be significant compared to the resolution of the instrument, and should be easily observed over the temperature range used.

Parameters	Temperature Dependence
Band overlap (meV): E_0	$= \begin{cases} -38 & (T < 80K) \\ -38 - 0.044(T-80) + 4.58\times10^{-4}(T-80)^2 - 7.39\times10^{-6}(T-80)^3 & (T > 80K) \end{cases}$
L-point direct band gap (meV): E_{gL}	$= 13.6 + 2.1\times10^{-3}T + 2.5\times10^{-4}T^2$
L-point electron: $m^*_{e,p}$	$= \dfrac{m^*(0)}{1 - 2.94\times10^{-3}T + 5.56\times10^{-7}T^2}$

Table 5.1: Temperature dependence of the band parameters in Bi

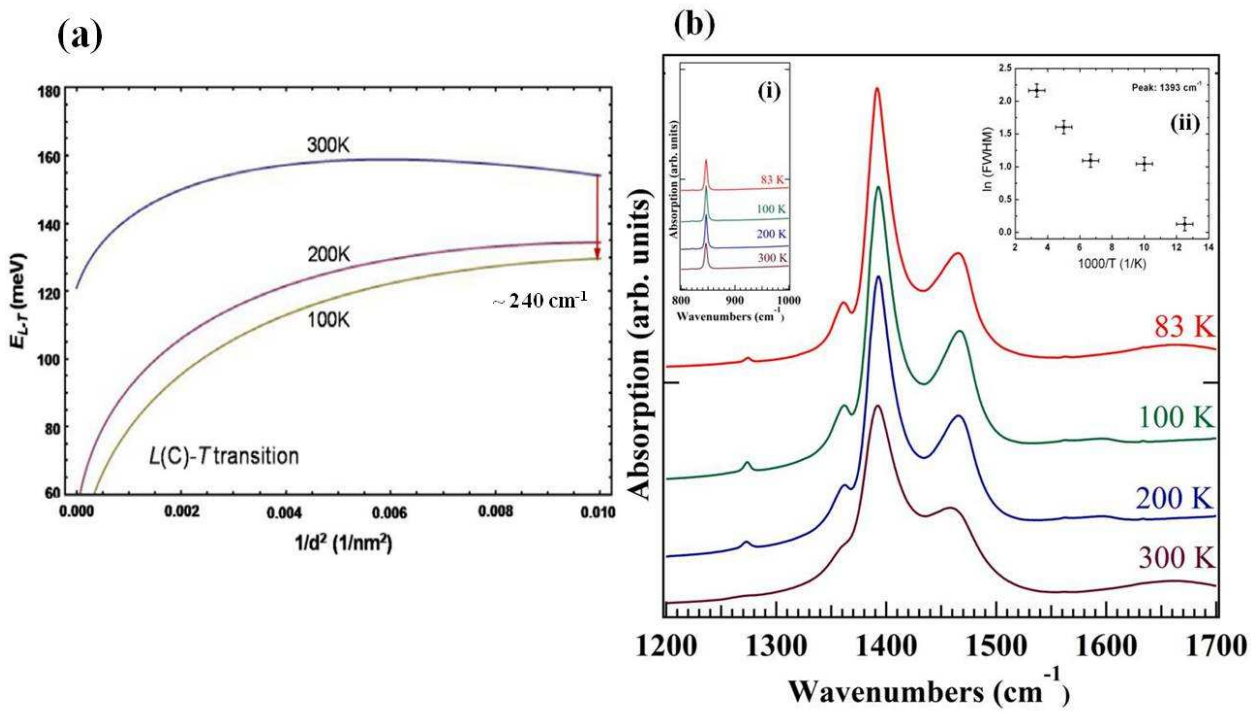

Figure 5.7: (a) Plot of $E_{L\text{-}T}$ vs $1/d^2$ for non parabolic model for *L(C)-T* transition as a function of temperature. (b) Experimentally observed spectra for 10 nm Bi nanorods as a function of temperature. Inset (i) shows the peak at 846 cm^{-1} and (ii) shows the linear trend of FWHM of 1393 cm^{-1} peak.

We conducted low temperature FTIR studies on the as-synthesized ~ 10 nm Bi nanorods, viz., the same Bi nanorods we used previously to perform room temperature IR spectroscopy study [99]. A modified Bruker FTIR spectrometer (model IFS 66v/s) equipped with a deuterated triglycine sulfate detector was used to collect the infrared absorption spectrum in the range of 400 – 4000 cm^{-1}. About 4 mg of the as-prepared Bi

nanorods (dia. ~10 nm) was mixed with ~96 mg of KBr powder and pressed into a 5 mm diameter pellet. A potassium bromide (KBr) beam splitter was used in the interferometer. The sample chamber was cooled down to 77 K and evacuated down to 1 mbar in order to eliminate the infrared absorption by the water vapor and CO_2 present in the ambient atmosphere. A platinum resistor (OMEGA Engineering, 2PT100KN3026) was used to measure the temperature at the sample.

Fig. 5.7b shows the corresponding temperature dependent FTIR spectra of 10 nm Bi nanorods. The absorption peak at 1393 cm^{-1} does not change position with changing temperature, although one would expect it t change if the peaks were due to the *L-T* transition. Meanwhile, the peak width changes as a function of temperature with an approximately 1/T behavior (inset (ii) of Fig. 5.7b). Along with the peak positions discussed so far for 10 nm Bi nanorods, another peak is also present at 846 cm^{-1} which was not identified in the previous work [99] [100]. This peak also does not shift as a function of temperature (Fig. 5.7b inset (i)). Although the result obtained from room temperature IR studies agrees well with the theory, the results obtained at low temperatures contradict the theoretical prediction of a red shifted *L-T* transition energy at low temperature.

As discussed in the introduction, theoretical studies predict a semimetal to semiconductor transition for Bi films of ~ 50 nm thickness [74]. Such predictions are based on bulk band structure parameters. But when the system is downsized to nanometer scale, significant

contributions from surface states are predicted [79, 80]. Bi nanorods differ from bulk Bi and are expected to have a high surface-to-volume ratio. Since Bi oxidizes rapidly, an oxide layer will be easily formed on the surface of the nanorods, for example, a ~2 nm oxide layer can be clearly seen in a ~ 10 nm Bi nanorod from its HR-TEM image in Fig. 5.4b [99]. In an effort to understand the origin of the IR absorption peaks in Bi nanorods, we also considered the presence of an oxide and/or carbonate layer on the surface of our nanorods since either Bi surface states or oxide/carbonate layers may explain the temperature independent nature of these absorption lines described in Fig. 5.7.

IR properties of Bi surfaces exposed to air

IR studies on Bi and Bi compounds

Spectroscopy is not only a very powerful tool to probe the electronic and vibrational properties of a material but also very sensitive to any contaminants present within or on the surface of the sample. It is well known that Bi readily oxidizes in air and can be contaminated quickly. In this section, we focus our discussion on the FTIR studies of micron size Bi powders and other Bi compounds. FTIR studies were performed using two different Bi samples. Figure 5.8a shows the spectrum of bulk Bi as obtained from Alfa Aesar. Extreme care was taken to prevent the exposure of the sample to the environment (referred as pure Bi). This sample does not have any signature in the mid infrared (MIR) region except for a sharp edge at ~ 560 cm^{-1}. In order to understand the size dependence

on the IR properties at the micron scale we ball-milled pure Bi for 1 h in a new container to prevent any cross contamination. The corresponding spectrum is shown in Fig. 5.8b. Even though ball-milling reduces the particle size from ~20 microns to ~2 microns and increases the surface-to-volume ratio, the FTIR spectrum of this sample did not show any significant change from that of the bulk sample. But if the bulk Bi sample is exposed to air, carbonate impurities present in the environment bond to the surface of Bi and its FTIR spectrum exhibits peaks at 846 cm^{-1}, 1393 cm^{-1} and 1460 cm^{-1} (Fig. 5.8c). These peaks have been identified to the presence of CO_3^{2-} ions [101]. We refer to this sample as contaminated Bi. Further confirmation for the presence of carbonate bonds is obtained by annealing the contaminated Bi sample in a CO_2 atmosphere. As can be seen in Fig. 5.8d, the peaks present in contaminated Bi increase in intensity and become more pronounced after annealing in CO_2. Similar studies were done by Noei *et. al.* who revealed IR spectral changes as a result of CO_2 absorption on ZnO nanoparticles [102].

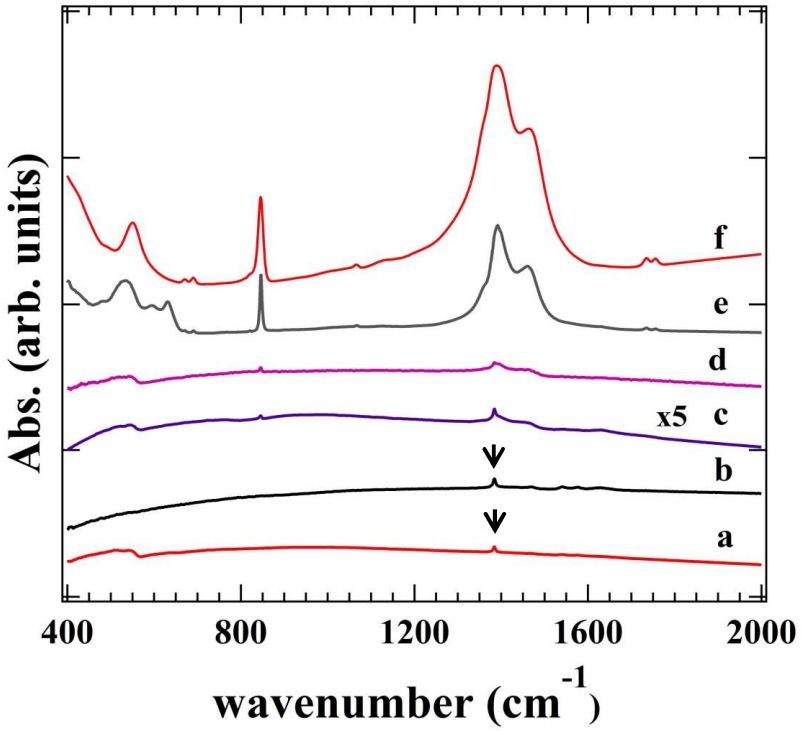

Figure 5.8: FTIR spectra of (a) Pure bulk Bi. (b) Ball-milled Bi. (c) Contaminated bulk Bi. (d) Contaminated Bi annealed in CO_2. (e) Bi nanorods, and (f) $Bi_2(CO_3)O_2$. The weak peak present at ~ 1384cm^{-1} and indicated by the down-pointing arrow corresponds a trace impurity phase present in the KBr powder.

On the other hand, similar annealing experiments in CO_2 atmosphere using pure Bi did not show any change in the IR spectrum. Interestingly, the energies corresponding to the peaks in contaminated Bi are very close to those attributed to the *L*-*T* transition energy in Bi nanorods (Fig. 5.8e). Hence, the peaks present in the IR spectrum of Bi nanorods may

be due to the bismuth-oxygen-carbon impurity phases rather than the *L-T* electronic transition. To cross check our results, we compared the FTIR data of 10 nm Bi nanorods (Fig. 5.8e) to that of bulk bismutite $Bi_2(CO_3)O_2$ as shown in Fig. 5.8f.

Clearly, the spectral features of Bi nanorods match with those of bismutite. Hence, we believe that the assignment of the peak at 1393 cm^{-1} observed in Bi nanorods to *L-T* transitions is not exclusively due to electronic transitions, and we conclude that this peak most likely originates from the bismuth-oxygen-carbonate phases present in the nanorods sample.

Photoacoustic Spectroscopy

As a sensitive probe, infrared spectroscopy is subject to many extrinsic perturbations. For example, Lovrincic *et. al.* [103] expressed concerns that the peaks we observed in the infrared spectrum of 10 nm Bi nanorods (Fig. 5.8e) may be due to impurity phases present in the KBr powder. In order to further address the issue of impurity phases present in the KBr powder, we performed photoacoustic spectroscopy (PAS) on samples from the same batches we used in Fig. 5.8.

The principles and applications of PAS are well documented in the literature [104-106]. Briefly, the sample (without the need for preparing a KBr pellet) is excited by intensity modulated light. Non-radiative decay to the ground state leads to heat generation that is

modulated at the same frequency as the light intensity, which in turn leads to pressure oscillations at that frequency in the gas that surrounds the sample. The pressure oscillations are sensed by a microphone, processed, and plotted as a function of wave number. Since the pressure variations in the airtight cells is a result of non-radiative de-excitation and measured using a microphone, this technique is immune to noise from reflected, transmitted, and scattered light. In the present case, the FTIR PA spectra of Bi compounds in the 400 – 4000 cm^{-1} were acquired by co-adding 384 scans at a resolution of 8 cm^{-1} using a Varian 7000 FTIR spectrometer equipped with a MTS300 photoacoustic module. The photoacoustic module consisted of a microphone with a nominal sensitivity of 50 mV/Pa and a sample cup of 10 mm diameter. The sample cup contained helium gas to enhance the signal amplitude. The spectrometer included a water cooled mid-IR source and KBr beam splitter. Rapid scan was used to obtain the spectra in the solid state. Since, the samples studied in PAS are not mixed with any other reference material (like KBr for FTIR absorption studies) all measured spectral features are intrinsic to the sample. The final spectra were normalized using PA signals from a carbon black pellet under the same experimental conditions. It can be clearly seen from Fig. 5.9 that the PA spectra exactly matched with the FTIR spectra shown in Fig. 5.8. This further confirms our conclusion that the peaks observed in the FTIR spectrum of Bi nanorods indeed arise from the bismuth-oxygen-carbon phases present in the sample.

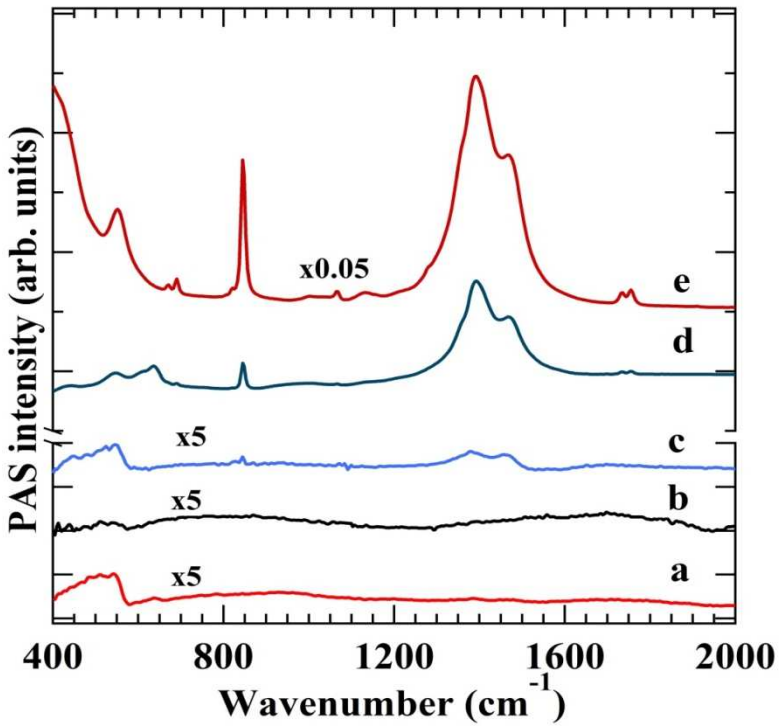

Figure 5.9: PA spectra of (a) Pure bulk Bi. (b) Ball-milled Bi. (c) Contaminated bulk Bi. (d) Bi nanorods, and (e) $(BiO)_2CO_3$. Notice that the impurity peak indicated by the down pointing arrow in Fig. 5.8 is absent in this data set.

In addition to the spectral features discussed so far, a sharp edge at low frequency (~ 560 cm^{-1}) is evident in both FTIR and PA spectra and is present in nearly all samples. Since, PAS studies are done on polycrystalline bulk powders, this absorption edge may be due to one or more possible transitions that occur due to the complicated Fermi surface of Bi. Tediosi *et. al.* studied the optical properties of single crystalline Bi and observed a similar feature at a slightly lower energy, which was attributed to the Drude edge [107].

Conclusions

In summary, theoretical modeling suggests that the electronic properties of Bi nanorods strongly depend on the nanorods diameter, and previous experimental studies confirmed these prediction through room temperature FTIR studies in which the *L-T* transition was tracked as a function of nanotube diameter (cf. Fig. 5.6). On the other hand, theoretical studies also predict temperature dependence for the *L-T* transition which was not observed in our low temperature FTIR studies. This led us to re-examine the origin of the FTIR features exhibited by the 10 nm Bi nanorods through a series of FTIR and PAS experiments conducted on pure, ball-milled, annealed Bi and bismutite samples. We finally conclude that the FTIR features assigned to *L-T* transition in 10 nm bismuth nanorods is most likely due to the oxygen-carbon impurities present on the surface of the sample.

FUTURE STUDIES

Understanding the electronic and vibrational properties of novel materials can provide insight into the physics of these materials and is very helpful from applications point of view. Electronically confined graphene structures such as graphene nanoribbons and graphene quantum dots offer excellent properties that would interest the scientific community. One of such properties is the photoluminescence which is absent in 2D structured graphene sheet due to lack of band gap. Although, our work experimentally determines the role of edge states in the PL behavior of GQDs, other factors such as the presence of defects, number of graphene layers in a GQD etc. could have huge role to play in the PL behavior of these quantum dots. On the other hand, GNRs have significant advantages when compared to GQDs; their dimensionality makes them suitable for application in electronics over GQDs and they also provide the much needed band gap. However, PL in graphene nanoribbons has not been explored in detail till date. Factors such as width of GNRs, number of graphene layers can significantly contribute to the PL behavior in this system.

Doping carbon systems such as SWNTs with a foreign element is known to have significant effect on the properties of these materials due to the change in energy band gap and symmetry lowering that can lead to relaxation of selection rules. So, studying the effect of dopants on the PL behavior of GNRs and GQDs can be a very interesting and useful study.

APPENDIX

The spectroscopic signal from a sample often has several peaks buried under a huge envelope and is not very well resolved (e.g.: absorption spectrum of SWNTs, emission spectrum of graphene quantum dots). But each of the hidden peaks provides information related to electronic and vibrational properties of the sample, such as lifetime, phonon modes etc. Therefore, it is important to deconvolute each peak from the spectrum. This can be done using plotting software such as Igor pro or Origin

1) Depending on the physical significance of the observed spectrum, the line shape of the peaks has to be determined (in this work, Lorentzian line shape analysis is used). In case of emission, it has been found that most of the peaks are Lorentzian. So the Lorentzian line shape analysis is used in this study. However, in some cases for absorption or vibrational spectroscopy, other line shapes such as Gaussian, Fano or other lines shapes can also be used depending on the phonon and electron dynamics, depending on the physics of the transition that causes the peaks.

2) Most spectra require a baseline correction to reduce the asymmetry; this can be done by fitting the baseline to a linear, cubic or higher polynomial and subtracting the fit values from the spectrum. The choice of the baseline used again depends on the presumed physics of the experiment.

3) The number of peaks present in the spectrum has to be identified and the variables of a peak such as peak position, intensity and FWHM have to be manually guessed. These

values are stored in a new table created for fitting (e.g; fit values). In case of GQDs, the FWHM of the entire spectrum is ~ 100 nm and it is known that in similar carbon systems such as bucky balls, the FWHM of each peak is 30-40 nm. So, it was estimated that each PL peak in GQDs might have ateast 3 peaks.

4) The next step is to write a program and execute the function. Below is a sample code to fit 3 Lorentzian peaks and a linear baseline.

```
#include  <Multi-peak fitting 1.4>
Function Lorfit ( cw ,x )
Wave cw
Variable x
Variable sum
sum = cw[0] + x * cw[1]
sum = sum + cw[2]  / (1+((x-cw[3]) / cw[4])^2)
sum = sum + cw[5] / (1+((x-cw[6]) / cw[7])^2)
sum = sum + cw[8] / (1+((x-cw[9]) / cw[10])^2)
Return (sum)
End
```

Lorfit is the name given to the function. The first line of the code "sum = cw[0] + x * cw[1]" performs linear baseline correction to the spectrum. Cw[1] corresponds to the

slope of the baseline and cw[0] is the intercept and x is the value on the x axis (in case of GQDs, this is wavelength)

"sum = sum + cw[2] / (1+((x-cw[3]) / cw[4])^2)" fits the first peak identified in the spectrum to a Loretzian. Since the fit includes summation of the baseline, peak fitting is always performed with respect to the imaginary baseline. Cw[2], cw[3] and cw[4] are the intensity, peak position and FWHM respectively.

Similarly, the other two Lorentzians are fitted within the spectrum and the final values are always stored in "sum". Values cw[0] to cw[10] are manually predicted values that are saved in a table "fit values".

To perform a multi-peak analysis, the range of the spectrum to be fitted is selected using cursors. One goes to the analysis menu in Igor and selects curve fitting. In the menu, select the function type, in this case Lorfit, then select x and y axis of the spectrum. Click on the tab "Data options" and select cursors (this determines the fitting range). Next, click the coefficients tab and select the column name given (fit values) to the vales cw[0] to cw[10]. Then click do it.

The program is executed with the variables in the column "fit values" and the fitted graph will be overlapped on the original spectrum. Also, the values in the column "fit values' also change according to the output values from the program executed.

The accuracy of the fit can be determined from the residual values that are displayed in the command menu. After fitting the spectrum, the original spectrum and fit spectrum look alike and the peak details are not clearly resolved for data representation.

So, for data representation purposes, once a proper fit is obtained, each deconvoluted peak with its respective values for intensity, peak position and FWHM can be plotted separately on the same graph. Such a spectrum looks like spectrum in fig 4.5.

It should be noted that additions of more peaks in bound to give a better fit. However, one should also consider the physical significance of the fit values. For example, if more peaks were used to fit the data, some fit values might look unrealistic such as negative or zero FWHM, negative intensity or some random values. So, proper care should be taken in choosing the number of peaks.

REFERENCES

1. M. S. Dresselhaus, G.D., Ph. Avouris, ed. *Carbon naontubes, Advanced Topics in the Synthesis, Structure,Properties and Applications*. 2001, Springer: Berlin Heidelberg.

2. M. S. Dresselhaus, G.D., P. C. Eklund Science of Fullerenes and Carbon Nanotubes: Their Properties and Applications, 1996, Academic Press.

3. Dresselhaus, M.S., et al., *Electronic, thermal and mechanical properties of carbon nanotubes.* Philosophical Transactions of the Royal Society of London. Series A: Mathematical, Physical and Engineering Sciences, 2004. **362**(1823): p. 2065-2098.

4. Geim, A.K. and K.S. Novoselov, *The rise of graphene.* Nat Mater, 2007. **6**(3): p. 183-191.

5. Dresselhaus, M.S., et al., *Raman spectroscopy of carbon nanotubes.* Physics Reports, 2005. **409**(2): p. 47-99.

6. Ado Jorio, M.S.D., Riichiro Saito, Gene Dresselhaus, *Raman Spectroscopy in Graphene Related Systems*. 1 ed2011: Wiley-VCH.

7. Wallace, P.R., *The Band Theory of Graphite.* Physical Review, 1947. **71**(9): p. 622-634.

8. Jorio, A., et al., Characterizing carbon nanotube samples with resonance Raman scattering. New Journal of Physics, 2003. **5**(1): p. 139.

9. McDonald, T.J., et al., Kinetics of PL Quenching during Single-Walled Carbon Nanotube Rebundling and Diameter-Dependent Surfactant Interactions†. The Journal of Physical Chemistry B, 2006. **110**(50): p. 25339-25346.

10. Cooper, D.R., et al., *Experimental Review of Graphene.* ISRN Condensed Matter Physics, 2012. **2012**: p. 56.

11. Nakada, K., et al., Edge state in graphene ribbons: Nanometer size effect and edge shape dependence. Physical Review B, 1996. **54**(24): p. 17954-17961.

12. Terrones, H., et al., *The role of defects and doping in 2D graphene sheets and 1D nanoribbons.* Reports on Progress in Physics, 2012. **75**(6): p. 062501.

13. Sun, L., et al., From zigzag to armchair: the energetic stability, electronic and magnetic properties of chiral graphene nanoribbons with hydrogen-terminated edges. Journal of Physics: Condensed Matter, 2011. **23**(42): p. 425301.

14. Fox, M., *Optical Properties of Solids*. 2 ed2010, USA: Oxford University Press.

15. Kuzmany, H., Solid-State Spectroscopy: An Introduction. 2 ed2009: Springer.

16. Valeur, B., Molecular Fluorescence: Principles and Applications. 1 ed2001: Wiley-VCH.

17. Venkateswaran, U.D., et al., Probing the single-wall carbon nanotube bundle: Raman scattering under high pressure. Physical Review B, 1999. **59**(16): p. 10928-10934.

18. Rao, A.M., et al., Effect of van der Waals Interactions on the Raman Modes in Single Walled Carbon Nanotubes. Physical Review Letters, 2001. **86**(17): p. 3895-3898.

19. Bachilo, S.M., et al., Structure-Assigned Optical Spectra of Single-Walled Carbon Nanotubes. Science, 2002. **298**(5602): p. 2361-2366.

20. O'Connell, M.J., et al., Band Gap Fluorescence from Individual Single-Walled Carbon Nanotubes. Science, 2002. **297**(5581): p. 593-596.

21. Pichler, T., et al., Localized and Delocalized Electronic States in Single-Wall Carbon Nanotubes. Physical Review Letters, 1998. **80**(21): p. 4729.

22. Landi, B.J., et al., *Purity Assessment of Single-Wall Carbon Nanotubes, Using Optical Absorption Spectroscopy.* The Journal of Physical Chemistry B, 2005. **109**(20): p. 9952-9965.

23. Terrones, M., Science and technology of the twenty-first century: Synthesis, properties and applications of carbon nanotubes. Annual Review of Materials Research, 2003. **33**: p. 419-501.

24. Podila, R., et al., Curvature-induced symmetry lowering and anomalous dispersion of the G-band in carbon nanotubes. Carbon, 2011. **49**(3): p. 869-876.

25. Rance, G.A., et al., UV-vis absorption spectroscopy of carbon nanotubes: Relationship between the [pi]-electron plasmon and nanotube diameter. Chemical Physics Letters, 2010. **493**(1-3): p. 19-23.

26. Lin, M.F. and D.S. Chuu, *pi plasmons in carbon nanotube bundles.* Physical Review B, 1998. **57**(16): p. 10183-87.

27. G. Dresselhaus, M.A.P., R. Saito, J.-C. Charlier, S. D. M. Brown, P. Corio, A. Marucci, and M. S. Dresselhaus, ed. *On the pi-pi overlap energy in carbon nanotubes*. Science and Applications of Nanotubes, ed. D.T.a.R.J. Enbody2000, Kluwer Academic: New York. 21.

28. Que, W., *Theory of plasmons in carbon nanotube bundles.* Journal of Physics: Condensed Matter, 2002. **14**(20): p. 5239.

29. Zoican Loebick, C., et al., *Selective Synthesis of Subnanometer Diameter Semiconducting Single-Walled Carbon Nanotubes.* Journal of the American Chemical Society, 2010. **132**(32): p. 11125-11131.

30. Arnold, M.S., et al., Sorting carbon nanotubes by electronic structure using density differentiation. Nat Nano, 2006. **1**(1): p. 60-65.

31. Lin, M.F., et al., *Collective excitations in a single-layer carbon nanotube.* Physical Review B, 1996. **53**(23): p. 15493-96.

32. Murakami, Y. and S. Maruyama, Effect of dielectric environment on the ultraviolet optical absorption of single-walled carbon nanotubes. Physical Review B, 2009. **79**(15): p. 155445.

33. Lin, M.F., C.S. Huang, and D.S. Chuu, *Plasmons in graphite and stage-1 graphite intercalation compounds.* Physical Review B, 1997. **55**(20): p. 13961-71.

34. Sun, Z., et al., Quantitative Evaluation of Surfactant-stabilized Single-walled Carbon Nanotubes: Dispersion Quality and Its Correlation with Zeta Potential. The Journal of Physical Chemistry C, 2008. **112**(29): p. 10692-10699.

35. Novoselov, K.S., et al., *Electric Field Effect in Atomically Thin Carbon Films.* Science, 2004. **306**(5696): p. 666-669.

36. Geim, A.K., *Graphene: Status and Prospects.* Science, 2009. **324**(5934): p. 1530-1534.

37. Lemme, M.C., et al., *A Graphene Field-Effect Device.* Electron Device Letters, IEEE, 2007. **28**(4): p. 282-284.

38. Han, M.Y., et al., *Energy Band-Gap Engineering of Graphene Nanoribbons.* Physical Review Letters, 2007. **98**(20): p. 206805.

39. Dimitrakopoulos, P.A.a.C., *Graphene: synthesis and applications - Review article.* Materials Today, 2010. **15**(3).

40. Mattevi, C., H. Kim, and M. Chhowalla, *A review of chemical vapour deposition of graphene on copper.* Journal of Materials Chemistry, 2011. **21**(10): p. 3324-3334.

41. Park, H.J., et al., Growth and properties of few-layer graphene prepared by chemical vapor deposition. Carbon, 2010. **48**(4): p. 1088-1094.

42. Gao, L.B.e.a., Repeated growth and bubbling transfer of graphene with millimetre-size single-crystal grains using platinum. Nat. Commun, 2012. **3**.

43. Lotya, M., et al., *Liquid Phase Production of Graphene by Exfoliation of Graphite in Surfactant/Water Solutions.* Journal of the American Chemical Society, 2009. **131**(10): p. 3611-3620.

44. Zhu, Y., et al., *Graphene and Graphene Oxide: Synthesis, Properties, and Applications.* Advanced Materials, 2010. **22**(35): p. 3906-3924.

45. Son, Y.-W., M.L. Cohen, and S.G. Louie, *Energy Gaps in Graphene Nanoribbons.* Physical Review Letters, 2006. **97**(21): p. 216803.

46. Barone, V., O. Hod, and G.E. Scuseria, *Electronic Structure and Stability of Semiconducting Graphene Nanoribbons.* Nano Letters, 2006. **6**(12): p. 2748-2754.

47. Yang, L., et al., *Quasiparticle Energies and Band Gaps in Graphene Nanoribbons.* Physical Review Letters, 2007. **99**(18): p. 186801.

48. Kosynkin, D.V., et al., Longitudinal unzipping of carbon nanotubes to form graphene nanoribbons. Nature, 2009. **458**(7240): p. 872-876.

49. Jiao, L., et al., *Narrow graphene nanoribbons from carbon nanotubes.* Nature, 2009. **458**(7240): p. 877-880.

50. Campos-Delgado, J., et al., Bulk Production of a New Form of sp2 Carbon: Crystalline Graphene Nanoribbons. Nano Letters, 2008. **8**(9): p. 2773-2778.

51. Cai, J., et al., Atomically precise bottom-up fabrication of graphene nanoribbons. Nature, 2010. **466**(7305): p. 470-473.

52. Pan, D., et al., Hydrothermal Route for Cutting Graphene Sheets into Blue-Luminescent Graphene Quantum Dots. Advanced Materials, 2010. **22**(6): p. 734-738.

53. Zhu, S., et al., Graphene quantum dots with controllable surface oxidation, tunable fluorescence and up-conversion emission. RSC Advances, 2012. **2**(7): p. 2717-2720.

54. Li, L.L., et al., A Facile Microwave Avenue to Electrochemiluminescent Two-Color Graphene Quantum Dots. Advanced Functional Materials, 2012: p. 2671-2679.

55. Li, Y., et al., An Electrochemical Avenue to Green-Luminescent Graphene Quantum Dots as Potential Electron-Acceptors for Photovoltaics. Advanced Materials, 2011. **23**(6): p. 776-780.

56. Peng, J., et al., *Graphene Quantum Dots Derived from Carbon Fibers.* Nano Letters, 2012. **12**(2): p. 844-849.

57. Dong, Y., et al., One-step and high yield simultaneous preparation of single- and multi-layer graphene quantum dots from CX-72 carbon black. Journal of Materials Chemistry, 2012. **22**(18): p. 8764-8766.

58. Liu, R., et al., *Bottom-Up Fabrication of Photoluminescent Graphene Quantum Dots with Uniform Morphology.* Journal of the American Chemical Society, 2011. **133**(39): p. 15221-15223.

59. Tang, L., et al., Deep Ultraviolet Photoluminescence of Water-Soluble Self-Passivated Graphene Quantum Dots. ACS Nano, 2012. **6**(6): p. 5102-5110.

60. Zhu, S., et al., Strongly green-photoluminescent graphene quantum dots for bioimaging applications. Chemical Communications, 2011. **47**(24): p. 6858-6860.

61. Lin, M.F., C.S. Huang, and D.S. Chuu, *Plasmons in graphite and stage-1 graphite intercalation compounds.* Physical Review B, 1997. **55**(20): p. 13961-13971.

62. Liu, C., et al., One-step synthesis of surface passivated carbon nanodots by microwave assisted pyrolysis for enhanced multicolor photoluminescence and bioimaging. Journal of Materials Chemistry, 2011. **21**(35): p. 13163-13167.

63. Gupta, V., et al., *Luminscent Graphene Quantum Dots for Organic Photovoltaic Devices.* Journal of the American Chemical Society, 2011. **133**(26): p. 9960-9963.

64. Neeleshwar, S., et al., *Size-dependent properties of CdSe quantum dots.* Physical Review B, 2005. **71**(20): p. 201307.

65. van Buuren, T., et al., Changes in the Electronic Properties of Si Nanocrystals as a Function of Particle Size. Physical Review Letters, 1998. **80**(17): p. 3803-3806.

66. Eda, G., et al., *Blue Photoluminescence from Chemically Derived Graphene Oxide.* Advanced Materials, 2010. **22**(4): p. 505-509.

67. Xu, Y.N., et al., Thermal Dynamics of Graphene Edges Investigated by Polarized Raman Spectroscopy. ACS Nano, 2010. **5**(1): p. 147-152.

68. Radovic, L.R. and B. Bockrath, On the Chemical Nature of Graphene Edges: Origin of Stability and Potential for Magnetism in Carbon Materials. Journal of the American Chemical Society, 2005. **127**(16): p. 5917-5927.

69. Smith, G.E., G.A. Baraff, and J.M. Rowell, *Effective g Factor of Electrons and Holes in Bismuth.* Physical Review, 1964. **135**(4A): p. A1118.

70. Giura, M., et al., *Singularities on the Fermi Surface of Bismuth.* Physical Review, 1969. **179**(3): p. 645.

71. Cankurtaran, M. and et al., *Energy bands, carrier density and Fermi energy in Bi in a uniform magnetic field.* Journal of Physics C: Solid State Physics, 1987. **20**(25): p. 3875.

72. Boyle, W.S. and A.D. Brailsford, *Far Infrared Studies of Bismuth.* Physical Review, 1960. **120**(6): p. 1943.

73. Reppert, J.B., synthesis and spectroscopic characterization of nanostructured thermoelectric materials in Materials Science and Engineering 2009, Clemson university: Clemson.

74. Lin, Y.-M., X. Sun, and M.S. Dresselhaus, Theoretical investigation of thermoelectric transport properties of cylindrical Bi nanowires. Physical Review B, 2000. **62**(7): p. 4610.

75. Lin, Y.-M., et al., *Transport properties of Bi nanowire arrays.* Applied Physics Letters, 2000. **76**(26): p. 3944-3946.

76. Asahi, H., T. Humoto, and A. Kawazu, *Quantum size effect in thin bismuth films.* Physical Review B, 1974. **9**(8): p. 3347-3356.

77. Hirahara, T., et al., Role of Spin-Orbit Coupling and Hybridization Effects in the Electronic Structure of Ultrathin Bi Films. Physical Review Letters, 2006. **97**(14): p. 146803.

78. Hasan, M.Z. and C.L. Kane, *Colloquium: Topological insulators.* Reviews of Modern Physics, 2010. **82**(4): p. 3045-3067.

79. Wells, J.W., et al., Nondegenerate Metallic States on Bi(114): A One-Dimensional Topological Metal. Physical Review Letters, 2009. **102**(9): p. 096802.

80. Koroteev, Y.M., et al., *Strong Spin-Orbit Splitting on Bi Surfaces.* Physical Review Letters, 2004. **93**(4): p. 046403.

81. Pascual, J.I., et al., *Role of Spin in Quasiparticle Interference.* Physical Review Letters, 2004. **93**(19): p. 196802.

82. Black, M.R., et al., Infrared absorption in bismuth nanowires resulting from quantum confinement. Physical Review B, 2002. **65**(19): p. 195417.

83. Levin, A.J., M.R. Black, and M.S. Dresselhaus, *Indirect L to T point optical transition in bismuth nanowires.* Physical Review B, 2009. **79**(16): p. 165117.

84. Cornelius, T.W., et al., *Quantum size effects manifest in infrared spectra of single bismuth nanowires.* Applied Physics Letters, 2006. **88**(10): p. 103114-3.

85. Vecchi, M.P. and M.S. Dresselhaus, *Temperature dependence of the band parameters of bismuth.* Physical Review B, 1974. **10**(2): p. 771.

86. Li, Y., et al., *Bismuth Nanotubes: A Rational Low-Temperature Synthetic Route.* Journal of the American Chemical Society, 2001. **123**(40): p. 9904-9905.

87. Derrouiche, S., C.Z. Loebick, and L. Pfefferle, *Optimization of Routes for the Synthesis of Bismuth Nanotubes: Implications for Nanostructure Form and Selectivity.* The Journal of Physical Chemistry C, 2010. **114**(8): p. 3431-3440.

88. Shim, W., et al., On-Film Formation of Bi Nanowires with Extraordinary Electron Mobility. Nano Letters, 2008. **9**(1): p. 18-22.

89. Lee, S. and et al., Direct observation of the semimetal-to-semiconductor transition of individual single-crystal bismuth nanowires grown by on-film formation of nanowires. Nanotechnology, 2010. **21**(40): p. 405701.

90. Heremans, J., et al., *Bismuth nanowire arrays: Synthesis and galvanomagnetic properties.* Physical Review B, 2000. **61**(4): p. 2921.

91. Black, M.R., et al., *Optical absorption from an indirect transition in bismuth nanowires.* Physical Review B, 2003. **68**(23): p. 235417.

92. Wang, Y.W., et al., Quantum size effects in the volume plasmon excitation of bismuth nanoparticles investigated by electron energy loss spectroscopy. Applied Physics Letters, 2006. **88**(14): p. 143106-3.

93. Rogacheva, E.I., S.G. Lyubchenko, and M.S. Dresselhaus, *Semimetal-semiconductor transition in thin Bi films.* Thin Solid Films, 2008. **516**(10): p. 3411-3415.

94. O'Sullivan, J.P. and G.C. Wood, *The Morphology and Mechanism of Formation of Porous Anodic Films on Aluminium.* Proceedings of the Royal Society of London. A. Mathematical and Physical Sciences, 1970. **317**(1531): p. 511-543.

95. Diggle, J.W., T.C. Downie, and C.W. Goulding, *Anodic oxide films on aluminum.* Chemical Reviews, 1969. **69**(3): p. 365-405.

96. Li, F., L. Zhang, and R.M. Metzger, *On the Growth of Highly Ordered Pores in Anodized Aluminum Oxide.* Chemistry of Materials, 1998. **10**(9): p. 2470-2480.

97. Z. Zhang, J.Y., and M. Dresselhaus, Bismuth quantum-wire arrays fabricated by a vacuum meltingand pressure injection process. Journal of materials research, 1998. **13**(7): p. 4.

98. Huber, T.E., et al., *Confinement effects and surface-induced charge carriers in Bi quantum wires.* Applied Physics Letters, 2004. **84**(8): p. 1326-1328.

99. Reppert, J., et al., *Laser-assisted synthesis and optical properties of bismuth nanorods.* Chemical Physics Letters, 2007. **442**(4-6): p. 334-338.

100. Levin, A.J., et al., Reply to "Comment on 'Indirect L to T point optical transition in bismuth nanowires'□". Physical Review B, 2010. **81**(19): p. 197102.

101. Tobon- Zapata, G.E., S.B. Etcheverry, and E.J. Baran, *Vibrational spectrum of bismuth subcarbonate.* Journal of Materials Science Letters, 1997. **16**(8): p. 656-657.

102. Noei, H., et al., Activation of Carbon Dioxide on ZnO Nanoparticles Studied by Vibrational Spectroscopy†. The Journal of Physical Chemistry C, 2010. **115**(4): p. 908-914.

103. Lovrincic, R. and A. Pucci, *Comment on "Indirect L to T point optical transition in bismuth nanowires"*. Physical Review B, 2010. **81**(19): p. 197101.

104. Griffiths, J.M.C.a.P.R., ed. *Handbook of Vibrational Spectroscopy*. 2002, John Wiley & Sons: New York.

105. Kuthirummal, N., *Listening to Nanomaterials: Photoacoustic Spectroscopy.* Journal of Chemical Education, 2009. **86**(10): p. 1238.

106. Rosencwaig, A., *Photoacoustics and photoacoustic Spectroscopy*1990: John Wiley & Sons Inc.

107. Tediosi, R., et al., Charge Carrier Interaction with a Purely Electronic Collective Mode: Plasmarons and the Infrared Response of Elemental Bismuth. Physical Review Letters, 2007. **99**(1): p. 016406.